Mycobacterial Metallophosphatase MmpE acts as a Nucleomodulin to Regulate Host Gene Expression and Promote Intracellular Survival

Liu Chen[1,2], Baojie Duan[1], Qiang Jiang[1], Yifan Wang[1], Yingyu Chen[1,3], Lei Zhang[1,3]* and Aizhen Guo[1,2,3]*

[1] National Key Laboratory of Agricultural Microbiology, College of Veterinary Medicine, Huazhong Agricultural University, Wuhan 430070, China

[2] Hubei Hongshan Laboratory, Huazhong Agricultural University, Wuhan 430070, China

[3] National Professional Laboratory for Animal Tuberculosis, Ministry of Agriculture and Rural Affairs, Huazhong Agricultural University, Wuhan 430070, China

*Address correspondence to: Lei Zhang, zhanglei2023@mail.hzau.edu.cn; Aizhen Guo, aizhen@mail.hzau.edu.cn

Abstract

Mycobacterium tuberculosis, the causative agent of tuberculosis, remains a major global health challenge. Nucleomodulins, bacterial effectors that target the host cell nuclei, are increasingly recognized as key virulence factors, but their roles in mycobacterial pathogenesis remain incompletely elucidated. Here, we characterize a hypothetical protein Rv2577 (designated MmpE) not only as a Fe^{3+}/Zn^{2+}-dependent metallophosphatase but also as a critical nucleomodulin involved in immune evasion and intracellular persistence. MmpE utilizes two nuclear localization signals, RRR^{20-22} and $RRK^{460-462}$, to enter the host cell nucleus, where it binds to the promoter region of the vitamin D receptor (VDR) gene, thereby inhibiting host inflammatory gene expression. Additionally, MmpE regulates the PI3K-Akt-mTOR signaling pathway, thereby arresting lysosome maturation. These actions collectively facilitate immune suppression and promote mycobacterial survival in macrophages and in mice. Our findings identify MmpE as a conserved nucleomodulin in mycobacteria and reveal a novel mechanism of MmpE-mediated intracellular survival.

Keywords Mycobacterium; Nucleomodulin; Metallophosphatase; Immune evasion; Intracellular survival.

Introduction

Mycobacterium tuberculosis (Mtb), the etiological agent of tuberculosis, has posed a persistent global health burden for centuries. Despite significant advances in elucidating the molecular mechanisms of its pathogenesis, current research has largely focused on effector proteins that modulate host cell membrane and cytoplasmic processes (Nisa *et al.,* 2022; Nasiri and Venketaraman, 2025). In contrast, investigations into effector proteins that target the host cell nucleus, the central hub for gene regulation and cellular control, remain comparatively limited.

Nucleomodulins are a class of bacterial effector proteins that can translocate into the host nucleus, where they modulate nuclear processes to promote pathogen survival (Chai *et al.,* 2020; Bierne and Cossart, 2021). These proteins affect host gene

29 expression by directly interacting with chromatin or by mimicking transcription factors,
30 chromatin modifiers, or other nuclear regulators (Li *et al.,* 2013; Rolando *et al.,* 2013;
31 Mitra *et al.,* 2018; Hanford *et al.,* 2021). For instance, LntA from *Listeria*
32 *monocytogenes* directly binds the chromatin repressor BAHD1, disrupting its function
33 and derepressing interferon-stimulated genes in a type III interferon-dependent
34 manner, ultimately promoting bacterial persistence (Lebreton *et al.,* 2011; Lebreton *et*
35 *al.,* 2014). Similarly, Ank1 and Ank6 from *Orientia tsutsugamushi* localize to the host
36 nucleus and facilitate the export of the NF-κB p65 subunit via exportin 1, thereby
37 suppressing the transcription of pro-inflammatory genes (Evans *et al.,* 2018; Steiert
38 and Weber, 2025). Although bacterial nucleomodulins utilize diverse strategies to
39 manipulate host nuclear functions, the identity and functional characterization of *M.*
40 *tuberculosis* nucleomodulins remain poorly defined.

41 Nucleomodulins employ various strategies to enter access to the host cell nucleus,
42 including passive diffusion, hijacking host proteins that contain nuclear localization
43 signals (NLSs), or using of their own NLSs to interact with the nuclear pore complex
44 (Hanford *et al.,* 2021). Among these mechanisms, NLSs play a particularly important
45 role. Classical NLSs are further divided into monopartite (MP) and bipartite (BP) forms.
46 Monopartite NLSs consist of a single cluster of 4-8 basic residues, primarily lysine (K)
47 or arginine (R), with a typical consensus motif of K-K/R-X-K/R (Fontes *et al.,* 2000;
48 Kosugi *et al.,* 2009; Cautain *et al.,* 2015). Nuclear localization enables these effectors
49 to manipulate host gene expression, disrupt immune signaling, and reprogram cellular
50 processes to promote pathogen survival. For example, EspF from enteropathogenic
51 *Escherichia coli* contains an N-terminal NLS that directs it to the nucleolus, where it
52 interferes with ribosome biogenesis (Dean *et al.,* 2010; Singh *et al.,* 2018). NUE, a
53 SET domain-containing nucleomodulin secreted by *Chlamydia trachomatis*, also
54 possesses an NLS that mediates its nuclear localization, where it functions as a
55 histone lysine methyltransferase (HKMTase) targeting host histones H2B, H3, and H4
56 (Pennini *et al.,* 2010; Jermy, 2010).

57 Beyond their nuclear localization capabilities, some nucleomodulins directly affect host

immunity through intrinsic enzymatic activities (Agarwal *et al.,* 2012). For example, the nucleomodulin PtpA promotes Mtb survival within macrophages by dephosphorylating host cytoplasmic proteins (Wang *et al.,* 2017). NleC from *E. coli*, a Zn^{2+}-dependent metalloprotease, suppresses host immune responses by cleaving the p65 subunit of NF-κB in the cytoplasm, thereby inhibiting its nuclear translocation, and can enter the nucleus to reduce nuclear p65 levels, blocking NF-κB-dependent transcription of pro-inflammatory genes (Baruch *et al.,* 2011; Hodgson *et al.,* 2015). Among these enzymatically active nucleomodulins, purple acid phosphatases (PAPs) represent a distinct and functionally significant, yet underexplored, subclass within the metallophosphatase superfamily. PAPs are characterized by a conserved β-α-β-α-β fold and five signature motifs (DxG, GDXXY, GNH[D/E], VXXH, GHXH), which coordinate seven metal-ligating residues at a binuclear metal center (Rodriguez *et al.,* 2014; Bhadouria *et al.,* 2017; Bhadouria and Giri, 2022). These enzymes have been extensively studied in plants and mammals, where they are involved in key biological processes such as phosphorus metabolism and the generation of reactive oxygen species (Comba *et al.,* 2013; Feder *et al.,* 2020; Liu *et al.,* 2025). However, only a few bacterial PAPs have been identified, such as BcPAP from *Burkholderia cenocepacia*, and their functions remain largely unknown (Yeung *et al.,* 2009). Notably, in Mtb, MmpE is the only identified PAP protein (Schenk *et al.,* 2000), but its specific contribution to infection and pathogenesis remain elusive.

In this study, we characterized MmpE as a conserved nucleomodulin in mycobacteria and demonstrated its nuclear translocation mediated by two functional motifs. Nuclear-localized MmpE regulates host immune responses by repressing the vitamin D receptor (VDR), a key regulator of antimicrobial gene expression, and disrupting lysosome maturation through suppression of the PI3K-Akt-mTOR signaling pathway. Additionally, MmpE exhibits Fe^{3+}-dependent metallophosphatase activity, contributing to intracellular survival. These findings establish MmpE as a bifunctional effector that integrates immune modulation and enzymatic catalysis, underscoring its role in mycobacterial pathogenesis and potential as a therapeutic target.

87 **Results**

88 **NLSs are required for the nuclear translocation of MmpE**

89 In a prior study, we screened conserved nucleomodulins in Mtb and found that
90 hypothetical protein Rv2577 (MmpE) exhibits strong nuclear localization in HEK293T
91 cells (Chen *et al.,* 2025). Furthermore, we observed a time-dependent increase in
92 nuclear MmpE-EGFP levels in HEK293T cells (Figure 1A, Figure S1A). Nuclear-
93 cytoplasmic fractionation assays further confirmed these results, showing a
94 progressive enrichment of MmpE in the nucleus during the course of transfection
95 (Figure 1B), suggesting that MmpE might possess a nuclear translocation ability.

96 MmpE contains two putative nucleus localization signals, NLS1 (RRR^{20-22}) and
97 NLS2 ($RRK^{460-462}$) which are located in the loop regions of the MmpE structure
98 predicted by AlphaFold (Figure 1C). Deleting either the individual NLSs or both
99 simultaneously does not lead to a conformational change in the core structure (Figure
100 S1B). To assess the effects of NLSs on nuclear localization, we constructed NLS-
101 deleted mutants, including $MmpE^{\Delta NLS1}$, $MmpE^{\Delta NLS2}$, and $MmpE^{\Delta NLS1-2}$ and transfected
102 them into HEK293T cells. Fluorescence microscopy at 36 hours post-transfection (hpt)
103 revealed that deletion of either NLS significantly reduced nuclear accumulation of
104 MmpE-EGFP, while simultaneous deletion of both NLS motifs ($MmpE^{\Delta NLS1-2}$)
105 completely abolished nuclear localization, resulting in exclusive cytoplasmic
106 distribution (Figure 1D and E). Consistent with the microscopy results, nuclear-
107 cytoplasmic fractionation showed that WT MmpE was present in detected both
108 cytoplasmic and nuclear fractions, whereas $MmpE^{\Delta NLS1}$ and $MmpE^{\Delta NLS2}$ exhibited
109 substantially reduced nuclear levels. Notably, the double mutant $MmpE^{\Delta NLS1-2}$ was
110 completely undetectable in the nucleus (Figure 1F and G), suggesting that both NLS
111 motifs are necessary for nuclear import.

112 To further detect whether MmpE translocates into the host nucleus during
113 mycobacterial infection, we conducted recombinant *M. bovis* BCG strains expressing
114 C-terminally Flag-tagged WT MmpE or the NLS deletion mutants including $MmpE^{\Delta NLS1}$,

115 MmpE$^{\Delta NLS2}$ and MmpE$^{\Delta NLS1\text{-}2}$. Immunoblot analysis of culture filtrates showed that both
116 MmpE-Flag and the secreted antigen Ag85B were detectable in the supernatant of
117 wild-type strains, whereas secretion of MmpE$^{\Delta NLS1}$ or MmpE$^{\Delta NLS1\text{-}2}$ was barely
118 detectable. These observations indicate that MmpE is secreted by BCG and that NLS1
119 is essential for its efficient export (Figure S1C). Following infection of THP-1
120 macrophages, nuclear-cytoplasmic fractionation revealed that wild-type MmpE
121 localized to both cytoplasmic and nuclear compartments, while MmpE$^{\Delta NLS1}$, MmpE$^{\Delta NLS2}$
122 or MmpE$^{\Delta NLS1\text{-}2}$ were almost undetectable in nuclear fractions (Figure S1D). These
123 findings indicate that nuclear localization of MmpE depends on two distinct NLS motifs,
124 with NLS2 being essential for effective nuclear translocation.

125 **Deletion of NLSs does not alter the phosphatase activity of MmpE**

126 MmpE is a putative a Fe^{3+}/Zn^{2+}-metallophosphatase with a purple acid phosphatase
127 (PAP) motif (Figure 2A; Figure S2A). Multiple sequence alignment and phylogenetic
128 reconstruction revealed that MmpE is highly conserved across mycobacterial species
129 and harbors canonical characteristics of metallophosphatases with GD, GNHX, and
130 GHXH motifs (Figure 2B, Figure S2B). These motifs are typically associated with
131 enzymes that catalyze phosphate hydrolysis via a binuclear metal ion-dependent
132 mechanism, wherein residues such as Asp, His, and Asn coordinate essential metal
133 cofactors, commonly Fe^{3+}, Mn^{2+}, or Zn^{2+}, at the active site. To test this, recombinant
134 MBP-tagged MmpE without the Tat signal peptide (MmpE$^{\Delta Tat}$) was purified and
135 subjected to *in vitro* phosphatase assays using *p*-nitrophenyl phosphate (*p*-NPP) as
136 the substrate. Different concentrations of Fe^{3+} or Zn^{2+} were added to the reactions to
137 detect their effects on the enzyme activity of MmpE. At the same ion concentrations,
138 Fe^{3+} is more effective than Zn^{2+} in stimulating MmpE hydrolysis of *p*-NPP. The maximal
139 enzymatic activity was observed at 50 μM Fe^{3+} (Figure 2C). To identify the key residues
140 of MmpE involved in metal coordination, molecular docking experiment was performed
141 using PyMOL on the structure of MmpE predicted by AlphaFold. His348 and Asn359
142 are supposed to be involved in metal ion coordination within the active site (Figure 2D).
143 Then, the double mutant MmpE$^{\Delta Tat}$-H348A/N359A was conducted to verify the

144 essential residues for enzyme activity. As shown in Figure 2E, the addition of 50 μM
145 Fe^{3+} significantly increased the *in vitro* phosphatase activity of $MmpE^{\Delta Tat}$ compared to
146 reactions without metal ions. However, the enzymatic activity of the $MmpE^{\Delta Tat}$-
147 H348A/N359A was significantly reduced under the same conditions, indicating that the
148 residues His348 and ASN359 are essential for metal binding and catalytic activity.
149 Additionally, we found that deletion of the NLSs does not affect the phosphatase
150 activity of MmpE (Figure 2F), consistent with the observation on comparison of the
151 structures (Figure S1B). Collectively, these results indicates that MmpE is a highly
152 conserved Fe^{3+}-dependent metallophosphatase in mycobacteria, and its enzymatic
153 activity is independent of the NLSs.

154 **The nuclear translocation and phosphatase activity of MmpE are essential for *M.***
155 ***bovis* BCG survival in macrophage cells**

156 To examine whether MmpE is important for bacterial intracellular survival, we
157 constructed *mmpE*-deletion mutant (ΔMmpE) in BCG strain by homologous
158 recombination (Figure S3A-C). The ΔMmpE mutant and the ΔMmpE strains
159 complemented with WT *mmpE* (Comp-MmpE) or NLS-deleted *mmpE* (Comp-
160 $MmpE^{\Delta NLS1}$, Comp-$MmpE^{\Delta NLS2}$, and Comp-$MmpE^{\Delta NLS1-2}$) exhibited similar growth rate
161 in the standard 7H9 media (Figure S3D). During infection of THP-1 macrophages, the
162 ΔMmpE strain exhibited a significantly reduced intracellular bacterial burden and
163 accelerated clearance compared to the WT strain, while this phenotype was restored
164 by complementation with wild-type MmpE. Importantly, the load of the Comp-
165 $MmpE^{\Delta NLS2}$ displayed significantly lower compared to Comp-MmpE in THP-1 cells
166 (Figure 3A). A comparable phenotype was also observed in RAW264.7 macrophages
167 (Figure 3B). These findings indicate that NLS2-mediated nuclear localization is critical
168 for the intracellular function of MmpE. Furthermore, the Comp-$MmpE^{\Delta NLS1}$ and Comp-
169 $MmpE^{\Delta NLS1-2}$ strains showed partial restoration of bacterial load compared to the
170 ΔMmpE strain, but remained lower than those of the Comp-MmpE strain (Figure 3C
171 and D). These results demonstrate that both NLSs are critical for MmpE-mediated
172 bacterial survival within macrophages. Given that MmpE functions as a Fe^{3+}-

173 dependent metallophosphatase in mycobacteria, we examined whether its enzymatic
174 activity contributes to intracellular persistence and constructed a phosphatase-
175 deficient double mutant strain (Comp-MmpE-H348A/N359A) (Figure S3E) to infect
176 THP-1 macrophage. The result showed that a significantly reduced intracellular
177 bacterial burden compared to Comp-MmpE, indicating that the phosphatase activity
178 also plays an important role in MmpE-mediated bacterial survival (Figure 3E). To
179 further investigate the underlying mechanism, we analyzed cytokine expression in
180 infected macrophages. Cells infected with the ΔMmpE and Comp-MmpE$^{\Delta NLS1-2}$ strains
181 exhibited significantly increased levels of pro-inflammatory cytokine, including *IL1A*,
182 *IL1B*, and *IL6*, compared to the WT and Comp-MmpE strains. Furthermore, in
183 comparison to the Comp-MmpE strains, cells infected with the Comp-MmpE$^{\Delta NLS1}$,
184 Comp-MmpE$^{\Delta NLS2}$, and Comp-MmpEH348A/N359A strains also demonstrated
185 substantial upregulation of these cytokines (Figure 3F-H). Collectively, these results
186 suggest that both nuclear localization and phosphatase activity are essential for the
187 immunomodulatory function of MmpE, which facilitates bacterial survival by
188 suppressing host inflammatory responses.

189 **MmpE regulates host transcription network involved in inflammation response**
190 **and lysosomal maturation**

191 To investigated the effect of MmpE on host gene expression, we performed RNA-seq
192 experiments on THP-1 macrophages infected with WT or ΔMmpE at 24 hpi. A total of
193 175 differentially expressed genes (DEGs) were identified, with 142 upregulated and
194 33 downregulated in ΔMmpE-infected cells compared to WT-infected cells (Figure 4A,
195 Table S2). Gene ontology (GO) analysis revealed significant enrichment in immune-
196 related biological processes, including apoptosis and cell death, molecular functions
197 associated with immune activation and cellular stress responses such as
198 pyrophosphatase activity and nucleoside-triphosphatase activity (Figure 4B). KEGG
199 pathway enrichment analysis showed that these DEGs were primarily involved in
200 immune and inflammatory signaling pathways, including cytokine-cytokine receptor
201 interaction, TNF, Toll-like receptor, chemokine, NF-κB, JAK-STAT, and PI3K-Akt

202 signaling pathways. Additionally, a subset of DEGs was involved in lysosome-
203 associated host pathways, consistent with previous findings that MmpE inhibits
204 lysosomal maturation (Forrellad *et al*., 2020) (Figure 4C). To further explore the
205 functional relevance of the DEGs, we performed protein-protein interaction (PPI)
206 network analysis focusing on protein-coding genes, which accounted for 38% of the
207 total DEGs (Figure S4C). The results suggested that some core proteins including
208 IL23A, IL12B, CSF2, CD69, IDO1, and CEACAM1, are mainly related to the production
209 of inflammatory cytokine and immune regulation (Figure 4D). Consistently, these
210 genes showed increased expression in ΔMmpE-infected macrophages compared to
211 those infected with wild-type BCG (Figure 4E). These results suggest that MmpE
212 suppresses immune and lysosome-associated gene expression during infection.

213 Further, we performed qRT-PCR to confirm the expression of key lysosomal
214 maturation markers, including *TFEB*, *LAMP1*, *LAMP2*, and several V-ATPase subunit
215 genes (*ATP6V0A1*, *ATP6V0C*, *ATP6V1A*, *ATP6V1B2*, and *ATP6V1E1*), as well as
216 inflammatory cytokine. The expression levels of these genes were significantly higher
217 in ΔMmpE-infected macrophages compared to those infected with WT (Figure 4F and
218 G). Moreover, infection with the Comp-MmpE$^{\Delta NLS1\text{-}2}$ strain resulted in significantly
219 increased gene expression compared to the Comp-MmpE strain (Figure S4B-D).
220 Taken together, these results suggest that MmpE suppresses host immune and
221 lysosomal responses to facilitate immune evasion during infection.

222 **MmpE regulates the PI3K-Akt-mTOR signaling pathway during macrophage**
223 **infection**

224 Given that MmpE modulates host transcriptional responses and functions as a
225 nucleomodulin, we investigated whether it associates with host chromatin to regulate
226 gene expression. Cleavage under targets and tagmentation (CUT&Tag) was
227 performed in HEK293T cells transfected with MmpE-EGFP. A total of 2,903 putative
228 MmpE-binding sites were identified (Table S3), of which 18.49% (n = 537) were located
229 in intergenic regions and 39.44% (n = 1,145) in intragenic regions (Figure 5A).
230 Chromosomal mapping revealed preferential enrichment on chromosomes 1 and 2

231 (Figure 5B). Notably, 99.7% (n = 2,894) of these binding sites were associated with
232 protein-coding genes, and 1,013 of them were located within 3 kb upstream of
233 transcription start sites (TSSs), including 63.18% within 1 kb, 22.9% between 1-2 kb,
234 and 13.92% between 2-3 kb (Figure 5C and D), suggesting that MmpE primarily targets
235 promoter regions to modulate transcription. PPI analysis of the 1,013 putative target
236 genes revealed significant enrichment in immune-related kinases genes, including
237 *PRKCB*, *PLCG2* and *PIK3CB*, which are key regulators of inflammatory signaling and
238 blockes lysosomal maturation via the PI3K-AKT-mTOR pathway (Tian *et al*., 2020;
239 Zheng et al., 2025) (Figure S5A and B). These findings are consistent with
240 transcriptomic analysis (Figure 4C) and support the hypothesis that MmpE modulates
241 host immune responses, potentially through the PI3K-AKT signaling axis. To validate
242 this hypothesis, we examined activation of the PI3K-AKT-mTOR pathway in THP-1
243 macrophages infected with either WT or ΔMmpE strains. Immunoblot analysis
244 demonstrated a time-dependent increase in the phosphorylation of AKT (Ser473),
245 mTOR (Ser2448), and p70S6K (Thr389) following WT infection, whereas
246 phosphorylation of these targets was attenuated in cells infected with the ΔMmpE
247 mutant (Figure S5C). To investigate the roles of nuclear localization and phosphatase
248 activity in MmpE-mediated signaling, THP-1 macrophages were infected with WT,
249 ΔMmpE, Comp-MmpE, Comp-MmpE$^{\Delta NLS1}$, Comp-MmpE$^{\Delta NLS2}$, Comp-MmpE$^{\Delta NLS1\text{-}2}$, or
250 Comp-MmpE-H348A/N359A. Cells infected with WT or Comp-MmpE exhibited
251 increased phosphorylation of Akt, mTOR, and p70S6K compared to those infected with
252 ΔMmpE and Comp-MmpE$^{\Delta NLS1\text{-}2}$ (Figure 5E and F). These results further indicate that
253 nuclear localization is the key determinant of MmpE-mediated activation of the PI3K-
254 AKT-mTOR pathway during mycobacterial infection.

255 As PI3K-Akt-mTOR signaling is known to inhibits phagolysosomal fusion (Yang *et*
256 *al*., 2020), and MmpE downregulates lysosomal genes (Figure 4G), we hypothesized
257 that MmpE may impair lysosomal maturation. To test this, we examined lysosomal
258 maturation in THP-1 macrophages infected with WT and mutant BCG strains by
259 confocal microscopy, using LysoTracker staining to assess lysosomal acidification. We

260 observed that ΔMmpE and MmpE^{NLS1-2} mutants exhibited significantly higher co-
261 localization with LysoTracker compared to WT and Comp-MmpE strains at 24 hpi
262 (Figure 5G), indicating that MmpE suppresses lysosomal maturation during infection.
263 To determine whether this effect is mediated through the PI3K-AKT-mTOR pathway,
264 THP-1 macrophages were treated with the dual PI3K/mTOR inhibitor BEZ235 at
265 concentrations ranging from 0 to 200 nM (Hsu *et al*., 2018). Growth assays confirmed
266 that BEZ235 had no effect on the viability of BCG strains over 8 days (Figure S6A).
267 However, under normal conditions, the ΔMmpE mutant exhibited approximately a 3-
268 fold reduction in intracellular survival compared to the wild-type strain. Upon BEZ235
269 treatment, this difference in bacterial load was substantially diminished (Figure S6B),
270 suggesting that PI3K-AKT-mTOR signaling contributes to MmpE-mediated immune
271 evasion. We further examined the intracellular survival of WT MmpE, NLS-deleted
272 mutant and phosphatase-inactive strains in THP-1 macrophages treated with 100 nM
273 BEZ235. Under untreated conditions, NLS-deficient and phosphatase-inactive strains
274 exhibited approximately a 2-fold reduction in intracellular survival compared to the WT
275 and complemented MmpE strains. This difference was abolished upon BEZ235
276 treatment (Figure S6C), further supporting the notion that activation of the PI3K-AKT-
277 mTOR pathway is essential for MmpE-mediated subversion of host antimicrobial
278 responses during mycobacterial infection.

279 **MmpE suppresses the expression of *VDR* during BCG infection**

280 Given the role of MmpE in modulating host signaling pathways, we next investigated
281 whether it directly targets specific host genes during macrophage infection. Focusing
282 on promoter regions (≤1 kb upstream of the transcription start site) of significantly
283 upregulated genes ($|Log_2FC > 1|$ and $P < 0.05$), we identified four candidate
284 transcription factors, including *CREBBP*, *VDR*, *GREB1*, and *FOXP4* (Figure 6A).
285 HOMER *de novo* motif analysis revealed a putative MmpE-binding motif specifically
286 with the promoter of *VDR*, a key anti-inflammatory gene (Aggeletopoulou *et al.,* 2022)
287 (Figure 6B). We next examined *VDR* expression in THP-1 macrophages infected with
288 recombinant strains. Compared to the WT, *VDR* expression was significantly

289 downregulated in cells infected with the ΔMmpE mutant (Figure 6C), suggesting that
290 MmpE suppresses *VDR* transcription. Furthermore, we cloned the *VDR* promoter
291 region (−100 bp to +50 bp) and conducted chromatin immunoprecipitation (ChIP)
292 assays in HEK293T cells. While both *VDR* and *GAPDH* sequences were detected in
293 input controls, *VDR* promoter DNA was selectively detected in ChIP samples from
294 MmpE-EGFP transfected cells (Figure 6D and E). In addition, the DNA-binding
295 capacity of MmpE was unaffected by its phosphatase activity (Figure 7F and G).
296 Electrophoretic mobility shift assays (EMSA) further confirmed the interaction,
297 demonstrating a shifted band corresponding to the MmpE-VDR promoter complex and
298 a dose-dependent increase in complex formation (Figure 7H and I). Collectively, these
299 results suggest that MmpE binds the VDR promoter to modulate its transcription.

300 To further characterize the MmpE-regulated transcriptional network, we integrated
301 CUT&Tag and RNA-seq data to identify 298 related genes (Table S4; Figure S7A and
302 B). GO enrichment analysis revealed that these genes were significantly enriched in
303 biological processes such as cell differentiation and regulation of small GTPase-
304 mediated signal transduction, both of which are fundamental to immune cell function,
305 trafficking, and inflammatory responses (Li *et al.,* 2023; Ma *et al.,* 2024) (Figure S7C
306 and D). These findings further establish MmpE as a nucleomodulin that rewires host
307 transcriptional programs involved in immune regulation and cellular defense.

308 **Nuclear translocation of MmpE is critical for mycobacterial survival in mice**

309 To investigate the role of MmpE as a nucleomodulin in vivo, C57BL/6 mice were
310 infected with WT, ΔMmpE, Comp-MmpE, and Comp-MmpE$^{\Delta NLS1\text{-}2}$ strains. Compared
311 with mice infected with WT or Comp-MmpE strains, mice infected with ΔMmpE or
312 Comp-MmpE$^{\Delta NLS1\text{-}2}$ strains had significantly lower bacterial loads in their lungs (Figure
313 7A). Similar results were observed in splenic bacterial colonization (Figure S8A).
314 Hematoxylin and eosin (H&E) staining of lung tissues from the mice infected with WT
315 or Comp-MmpE strains showed extensive inflammatory infiltrates, while the lungs of
316 the mice infected with ΔMmpE or Comp-MmpE$^{\Delta NLS1\text{-}2}$ strains exhibited markedly
317 reduced inflammation (Figure 7B). In addition, compared with mice infected with WT

318 or Comp-MmpE strains, mice infected with ΔMmpE or Comp-MmpE$^{\Delta NLS1-2}$ strains
319 showed a significant increase in *Il1a*, *Il1b*, and *Il6* in the spleen (Figure 7C and E).
320 These results indicate that the nuclear translocation of MmpE is critical for
321 mycobacterial intracellular survival.

322 Since MmpE modulates host transcriptional responses in THP-1 macrophages,
323 we examined the expression of *Vdr*, inflammation-related, and lysosome-associated
324 genes in the lungs and spleens of mice at 14 and 28 days post infection (dpi). *Vdr*
325 expression was significantly reduced in both lungs and spleens infected with the
326 ΔMmpE or Comp-MmpE$^{\Delta NLS1-2}$ strains compared to those infected with WT or Comp-
327 *MmpE* strains (Figure S8B). Consistent with H&E observation, the expression of
328 inflammation-related genes (e.g., *Il23a*, *Csf2*, *Cd69*, *Ido1*, *Il12b,* and *Ceacam1*) were
329 markedly decreased in lungs infected with the ΔMmpE or Comp-MmpE$^{\Delta NLS1-2}$, but
330 significantly elevated in spleens from the same groups (Figure S8C-D). Moreover, as
331 observed in vitro, lysosomal maturation-associated genes, such as *Tfeb*, *Lamp1*,
332 *Lamp2*, together with genes encoding V-ATPase subunits, were upregulated in both
333 lung and spleen tissues of the mice infected with ΔMmpE or Comp-MmpE$^{\Delta NLS1-2}$
334 (Figure S8E-H). Taken together, our experiments demonstrate that MmpE promotes
335 mycobacterial survival in vivo through its nuclear translocation, likely by modulating
336 host immune responses and lysosomal maturation pathways.

337 **Discussion**

338 **MmpE is a bifunctional virulence factor in Mtb**

339 Previously, Forrellad *et al*. (2020) characterized Rv2577/MmpE of Mtb as an alkaline
340 phosphatase/phosphodiesterase that affects phagosome maturation arrest and
341 virulence of Mtb. While the enzymatic activity and virulence-related phenotype of
342 MmpE have been established, specific cofactor dependencies, catalytic residues, and
343 the mechanisms underlying host-pathogen interactions remain inadequately defined.
344 Here, our study shows that MmpE possesses Fe^{3+}-dependent phosphatase activity,
345 with H348 and N359 identified as critical catalytic residues (Figure 2C-E). Moreover,

346 deletion of these residues significantly impairs the survival of recombinant BCG strains
347 in THP-1 macrophages, indicating that its phosphatase activity is essential for
348 intracellular persistence (Figure 3E). Furthermore, our study identifies MmpE as a
349 novel nucleomodulin that translocates into the host nucleus primarily via its nuclear
350 localization signal (NLS; $RRK^{460-462}$) (Figure 1D-G, Figure S1D). Upon infection, MmpE
351 modulates a broad range of host immune signaling pathways, including cytokine-
352 cytokine receptor interactions, TNF, Toll-like receptor, chemokine, NF-κB, JAK-STAT,
353 and PI3K-Akt pathways. Specifically, MmpE enhances the phosphorylation levels of
354 AKT (Ser473), mTOR (Ser2448), and p70S6K (Thr389), modulating the PI3K-AKT-
355 mTOR signaling pathway and ultimately impairing lysosomal maturation to promote
356 intracellular survival of the pathogen (Figure 5E and G, Figure S5C, Figure S6B and
357 C). Additionally, it also regulates the expression of key transcription factors, such as
358 VDR, CREBBP, GREB1, and FOXP4 (Figure 6A). Notably, the deletion of the NLS
359 significantly impairs the functionality of MmpE, thereby reducing the survival of BCG
360 strains in both macrophages and murine models (Figure 3A-D, Figure 7A). Taken
361 together, these findings indicate that MmpE functions as a bifunctional virulence factor,
362 combining phosphatase activity with nuclear localization to modulate host responses
363 during infection.

364 **Targeting host *VDR* gene might represent a unique immune evasion strategy by**
365 **Mtb.**

366 Nucleomodulins are effector proteins secreted by bacterial pathogens that specifically
367 target the host cell nucleus, where they modulate nuclear processes to subvert host
368 responses (Hanford *er al*., 2021). Their mechanisms of action within the nucleus
369 typically involve indirect interference with host transcriptional programs, such as
370 through epigenetic modifications, chromatin remodeling, or inhibition of key signaling
371 pathways (Jose *et al.,* 2016; Singh *et al.,* 2023). Despite extensive characterization of
372 nucleomodulin functions, direct binding to host gene promoters remains rare and
373 mechanistically distinct. In this study, we found that MmpE directly binds to the
374 promoter of the *VDR* gene (Figure 6) and attenuates the expression of VDR-regulated

375 inflammatory genes (Zhou *et al*., 2020; Yang *et al*., 2019) (Figure 3F-H). VDR is a
376 critical nuclear receptor that controls the expression of numerous genes involved in
377 host immune defense, including antimicrobial peptides and cytokine (Usategui-Martín
378 *et al.,* 2022). For example, Mtb suppresses the expression of the host gene *CYP27B1*
379 to reduce active vitamin D synthesis, thereby limiting VDR activation and downstream
380 antimicrobial responses (Liu *et al.,* 2006). Similarly, *Salmonella* downregulates *VDR*
381 through miRNA-mediated mechanisms, weakening mucosal immunity (Chen *et al.,*
382 2014). This mechanism of MmpE regulating VDR expression reveals a novel strategy
383 by bacterial pathogens to evade host defenses through direct manipulation of host
384 gene promoters by nucleomodulins.

385 **MmpE regulates the PI3K-Akt-mTOR pathway to inhibit lysosomal maturation**
386 **and enhance pathogen survival.**

387 Mtb employs multiple strategies to evade phagolysosomal degradation, a process
388 essential for bacterial clearance (Chandra *et al.,* 2022; Zhang *et al.,* 2023; Singh and
389 Nagaraja, 2025). For example, approximately 70% of phagosomes harboring Mtb fail
390 to fuse with lysosomes, partly due to the activity of secreted phosphatases such as
391 PtpA, PknG, and SapM, which disrupt vesicular trafficking (Wong *et al.,* 2011; Ge *et*
392 *al.,* 2022; Zhang *et al.,* 2024; Alsayed and Gunosewoyo, 2024). MmpE has also been
393 shown to contribute to the arrest of lysosomal maturation in human cells; however, the
394 underlying mechanisms remain unclear (Forrellad *et al.,* 2020).

395 In this study, we elucidate a mechanism by which MmpE inhibits lysosomal
396 maturation. The absence of MmpE during BCG infection resulted in substantial
397 upregulation of lysosome-associated genes, including *TFEB*, a master regulator of
398 lysosomal biogenesis and function, underscoring MmpE's role in lysosomal regulation
399 (Jeong *et al*., 2021; Wang *et al*., 2024) (Figure 4G, Figure S4C). Moreover, the ΔMmpE
400 and MmpE$^{\Delta NLS1\text{-}2}$ mutants exhibited significantly increased expression of lysosomal
401 maturation-associated genes in both mice and infected THP-1 cells, along with
402 enhanced LysoTracker co-localization in THP-1 cells, compared to WT and Comp-
403 MmpE strains (Figure 4G, Figure 5G, Figure S8C-F). Collectively, these findings

404 indicate that MmpE inhibits lysosomal maturation during mycobacterial infection.
405 Furthermore, CUT&Tag analysis revealed that MmpE binds to the promoter regions of
406 host genes within the PI3K-Akt-mTOR signaling pathway, including *PRKCB*, *PLCG2*,
407 and *PIK3CB*, which are key upstream regulators of TFEB activity (Fang *et al.,* 2021;
408 Gounis *et al.,* 2025) (Figure S5A). Additionally, during infection, WT strains exhibited
409 significantly elevated phosphorylation of Akt, mTOR, and p70S6K compared to the
410 ΔMmpE and the Comp-MmpE$^{\Delta NLS1\text{-}2}$ strain (Figure 5E-F, Figure S5C). When THP-1
411 macrophages were treated with the dual PI3K/mTOR inhibitor BEZ235, the survival
412 difference between WT and MmpE mutants was significantly reduced (Figure S6B-C).
413 These results collectively indicate that MmpE regulates the PI3K-Akt-mTOR-TFEB
414 axis, thereby inhibiting lysosomal maturation and enhancing bacterial survival in the
415 host.

416 In summary, our study identifies MmpE as a novel bifunctional virulence factor of
417 mycobacteria, combining Fe^{3+}-dependent phosphatase activity with nuclear
418 translocation capability. MmpE translocates into the host nucleus and directly binds to
419 the promoters of some key host genes, such as *VDR*, thereby inhibiting the expression
420 of the downstream targets implicated with the inflammation responses and lysosomal
421 maturation, thereby promoting mycobacterial survival in macrophages and in mice
422 (Figure 8). These findings reveal a sophisticated mechanism by which bacterial
423 pathogen manipulates host gene transcription and signaling pathway to promote
424 intracellular persistence.

425 **Materials and methods**

426 **Bacterial strains and culture conditions**

427 The bacterial strains used in this study are detailed in Table S6. *E. coli* DH5α and BL21
428 were cultured in Luria-Bertani (LB) medium under standard conditions. *M. bovis* BCG
429 strains were grown in Middlebrook 7H9 broth supplemented with 10% (v/v) OADC
430 (oleic acid, albumin, dextrose, catalase), 0.05% (v/v) Tween-80, and 2% (v/v) glycerol.
431 Antibiotics were added as required at the following final concentrations: 50 μg/mL
432 hygromycin (for mycobacteria) and 50 μg/mL kanamycin (for both mycobacteria and *E.*

433 *coli*).

434 **Cell culture**

435 THP-1 cells were cultured in Roswell Park memorial institute 1640 (RPMI 1640)
436 medium supplemented with 10% (v/v) heat-inactivated fetal bovine serum (FBS), 1 mM
437 sodium pyruvate, 2 mM L-glutamine, 10 mM HEPES buffer (pH 7.2-7.5), and 50 μM 2-
438 mercaptoethanol. For differentiation into macrophages, THP-1 cells were treated with
439 200 nM phorbol 12-myristate 13-acetate (PMA) for 24 h to allow complete
440 differentiation prior to experimental use.

441 HEK293T cells and RAW264.7 macrophages were cultured in Dulbecco's modified
442 Eagle's medium (DMEM) supplemented with 10% (v/v) FBS and 50 μg/mL penicillin-
443 streptomycin. All cells were maintained at 37 °C in a humidified atmosphere with 5%
444 CO_2.

445 **Animal experiments**

446 Specific pathogen-free (SPF) female C57BL/6 mice (6-8 weeks old, 16-18 g) were
447 obtained from Chang-sheng Bio (Liaoning, China). All animals were maintained under
448 SPF conditions in individually ventilated cages with controlled temperature and
449 humidity, on a 12-hour light/dark cycle. Mice had ad libitum access to sterilized food
450 and water.

451 **Phylogenetic and sequence analysis**

452 Homologs of the metallophosphatase MmpE were identified from 11 *Mycobacterium*
453 species, including *M. tuberculosis* (Mtu), *M. bovis* BCG (Mbb), *M. orygis* (Mory), *M.*
454 *kubicae* (Mku), *M. paraterrae* (Mpa), *M. farcinogenes* (Mfg), *M. mucogenicum* (Mmuc),
455 *M. vicinigordonae* (Mvg), *M. lentiflavum* (Mlf), *M. avium* (Mav), and *M. manitobense*
456 (Mman). Genomic sequences were retrieved from the NCBI RefSeq database and
457 filtered for completeness.

458 Protein sequences were aligned using Clustal Omega v1.2.4 with default parameters
459 (gap opening penalty = 10, gap extension = 0.2, and iterative refinement enabled).
460 Conserved residues (≥90% identity) were visualized using ESPript 3.0. Phylogenetic

461 reconstruction was performed in MEGA v12.0 using the neighbor-joining algorithm with
462 pairwise deletion for gap treatment and a Poisson substitution model, appropriate for
463 closely related bacterial sequences. Bootstrap support was calculated with 1,000
464 replicates, and nodes with values ⩾50% were retained. The resulting tree was
465 visualized using the iTOL platform, without additional pruning.

466 **Structural Analysis of MmpE**

467 Structural models of full-length MmpE and its NLS-deletion mutants ($MmpE^{\Delta NLS1}$,
468 $MmpE^{\Delta NLS2}$, $MmpE^{\Delta NLS1\text{-}2}$) were generated using AlphaFold v2.2.0. Predictions were
469 performed with default settings, including use of the pre-trained model and MSA
470 generation via UniRef90 and MGnify. Model confidence was assessed using pLDDT
471 scores. All structures were analyzed in UCSF ChimeraX for conformational differences
472 between mutants. The AlphaFold-predicted reference model was further examined in
473 PyMOL to identify putative metal-binding residues based on spatial proximity and
474 coordination geometry within the predicted active site.

475 **Cell transfection and confocal microscopy**

476 HEK293T cells were seeded at 70% confluency in poly-L-lysine-coated 35-mm glass-
477 bottom dishes and maintained in DMEM supplemented with 10% (v/v) FBS at 37 °C
478 with 5% CO_2. Transfection was performed using the Hieff Trans™ Liposomal
479 Transfection Reagent according to the manufacturer's protocol. Briefly, 0.5 μg of
480 plasmid DNA and 1.5 μL of transfection reagent were diluted in 250 μL of Opti-MEM,
481 incubated at room temperature for 20 minutes, and added dropwise to each well.

482 At 24-48 hpt, cells were washed with PBS, fixed in 4% paraformaldehyde for 15 min,
483 and permeabilized with 0.1% Triton X-100 for 10 min. Nuclei were counterstained with
484 1 μg/mL DAPI for 10 min. Imaging was performed using an Olympus FV1000 Confocal
485 Laser Scanning Microscope equipped with a 100×/1.40 NA oil immersion objective.
486 Fluorescence was detected using the following parameters: EGFP, excitation at
487 488 nm, emission at 509 nm; DAPI, excitation at 405 nm, emission at 461 nm. Spectral
488 unmixing was applied using FV10-ASW v4.2 to minimize channel cross-talk. Z-stack

489 images were acquired in sequential mode with a step size of 0.5 μm to ensure
490 consistency across samples.

491 **Cell fractionation and Immunoblotting**

492 Cells were lysed in RIPA buffer supplemented with 1 % (v/v) protease inhibitor cocktail,
493 and protein concentrations were determined using the BCA assay. Equal amounts of
494 protein were separated by SDS-PAGE and transferred onto PVDF membranes.
495 Membranes were blocked for 1 h at room temperature with 5% (w/v) non-fat milk in
496 TBST (25 mM Tris, 150 mM NaCl, 2 mM KCl, 0.2% Tween-20, pH 7.4), then incubated
497 overnight at 4 °C with primary antibodies. After three 6-min washes with TBST,
498 membranes were incubated with HRP-conjugated secondary antibodies for 1 h at room
499 temperature. Signal detection was performed using enhanced chemiluminescence
500 (ECL), and images were acquired with the ChemiDoc™ MP Imaging System (Bio-Rad).
501 For subcellular fractionation, nuclear and cytoplasmic protein fractions were prepared
502 using the Nuclear and Cytoplasmic Protein Extraction Kit (Beyotime) with minor
503 modifications. Cells were washed with PBS, detached using a cell scraper, and
504 pelleted by centrifugation at 2,000 × *g* for 5 min. The pellet (~20 μL packed cells) was
505 resuspended in 150 μL of Cytoplasmic Extraction Reagent A (with PMSF), vortexed for
506 5 s, and incubated on ice for 15 min. After addition of 10 μL Reagent B, the sample was
507 vortexed briefly, incubated on ice, and centrifuged at 12,000 × *g* for 5 min at 4 °C to
508 collect the cytoplasmic fraction (supernatant). The remaining pellet was extracted with
509 50 μL of Nuclear Extraction Reagent (with PMSF), vortexed intermittently for 30 min on
510 ice, and centrifuged at 12,000 × *g* for 10 min at 4 °C to obtain the nuclear fraction. β-
511 actin, or histone H3 was used as a loading control for cytoplasmic or nuclear fractions.
512 Antibody information is listed in the Table S1.

513 **Immunoblot analysis of MmpE secretion**

514 The procedure for immunoblot analysis of MmpE secretion was adapted from previous
515 studies with minor modifications (Zhang *et al*., 2022; Chen *et al*., 2025). BCG strains
516 expressing C-terminally Flag-tagged MmpE were cultured in Middlebrook 7H9 broth

517 with 0.5% glycerol, 0.02% Tyloxapol, and 50 μg/mL kanamycin at 37 °C (80 rpm) until
518 OD600 ~0.6. Cells were harvested by centrifugation (4,000 × *g*, 15 min, 4 °C), and
519 supernatants filtered through 0.22 μm PES membranes. Filtrates were concentrated
520 ~50-fold using Amicon Ultra-15 filters (10 kDa cutoff) for secreted MmpE detection.
521 Bacterial pellets were washed, resuspended in lysis buffer (50 mM Tris-HCl, pH 7.5;
522 150 mM NaCl; 1 mM PMSF; protease inhibitors). Lysates were clarified by
523 centrifugation (10,000 × *g*, 15 min, 4 °C). Whole-cell lysates and concentrated culture
524 filtrates were analyzed by immunoblotting as described above, using anti-Flag
525 antibodies for detection.

526 **Protein Expression and Purification**

527 N-terminal maltose-binding protein (MBP)-tagged and C-terminal His_6-tagged wild-
528 type MmpE, as well as mutant lacking the Tat signal peptide were expressed in *E. coli*
529 BL21 (DE3). Protein expression was performed in 1 L of LB medium. Cultures were
530 grown at 37 °C until the optical density at 600 nm (OD_{600}) reached approximately 0.8,
531 after which protein expression was induced with 0.2 mM IPTG at 18 °C for 24 h.
532 Following induction, cells were harvested by centrifugation and lysed by sonication in
533 ice-cold lysis buffer containing 150 mM NaCl, 30 mM Tris-HCl (pH 7.5), and 1 mM
534 PMSF. The lysate was clarified by centrifugation, and the supernatant was subjected
535 to affinity purification using an MBP affinity column.

536 **Phosphatase activity assay**

537 Phosphatase activity was measured using *p*-nitrophenyl phosphate (*p*-NPP) as the
538 substrate in a final reaction volume of 200 μL. Reactions were initiated by incubating
539 0-80 μg of purified protein with *p*-NPP at 37 °C for 60 min. The release of *p*-nitrophenol
540 (*p*-NP), the dephosphorylated product, was quantified by measuring absorbance at
541 405 nm using a microplate spectrophotometer.

542 Kinetic parameters were determined under initial velocity (V_0) conditions using
543 substrate concentrations ranging from 0.1 to 10 mM *p*-NPP. The kinetic constants Km
544 and Vmax were calculated by fitting the data to the Michaelis-Menten equation using
545 nonlinear regression analysis in GraphPad Prism 8.0. The catalytic turnover rate (Kcat)

546 was calculated using the equation Kcat = Vmax/E_0, where Vmax was expressed as
547 nM *p*-NP min^{-1} and E_0 represents the active enzyme concentration. Control reactions
548 were carried out in the absence of either the substrate or the enzyme to measure
549 background absorbance. All assays were performed in triplicate to ensure the
550 reproducibility of results.

551 **Quantitative real-time PCR**

552 THP-1 cells were infected with the BCG strain and harvested 24 hpi for total RNA
553 isolation. RNA was extracted using 1 mL of TRIzol® reagent following the
554 manufacturer's protocol. To eliminate genomic DNA contamination, RNA samples were
555 treated with DNase I for 30 min at 37 °C, followed by heat inactivation at 65 °C for 10
556 min. RNA concentration and purity were assessed using a NanoDrop 2000
557 spectrophotometer (Thermo Fisher Scientific).

558 For cDNA synthesis, 1 μg of total RNA was reverse transcribed using the HiScript® III
559 cDNA Reverse Transcription Kit with random hexamers primers, according to the
560 manufacturer's protocol. qRT-PCR was performed using ChamQ SYBR® Green RT-
561 PCR Master Mix. Relative mRNA expression levels were calculated using the $2^{-\Delta\Delta Ct}$
562 method, normalizing Ct values to the housekeeping gene *HPRT*. All qRT-PCR
563 experiments were conducted in triplicate, with at least three independent biological
564 replicates and two technical replicates per condition. Primer sequences are listed in
565 Table S7.

566 **RNA-seq analysis**

567 THP-1 cells were seeded at a density of 1 × 10^6 cells well in 6-well plates and
568 differentiated into macrophages by treatment with 100 nM PMA for 48 h. After
569 differentiation, cells were washed with PBS and infected with BCG WT or ΔMmpE
570 strains at a multiplicity of infection (MOI) of 10:1. Following 24 h of infection, total RNA
571 was extracted using TRIzol® reagent according to the manufacturer's protocol.

572 High-quality sequencing reads were then aligned to the human reference genome
573 (GRCh38) using HISAT2 (v2.2.1). Transcript quantification was performed using

574 FeatureCounts (v2.0.3), and differential gene expression analysis was conducted
575 using DESeq2 (v1.38.3) in R. Genes with an adjusted *P*-value < 0.05 and an absolute
576 $|\log_2$ fold change ≥ 1| were considered significantly differentially expressed. RNA-seq
577 data were visualized using GraphPad Prism version 8.0, as well as volcano plots,
578 heatmaps, and other graphical outputs generated via the SRplot platform (Tang *et al.,*
579 2023).

580 **CUT&Tag analysis**

581 HEK293T cells were seeded in 10 cm^2 dishes at a density of 1×10^7 cells per well and
582 transfected with 10 μg of the MmpE-pEGFP expression plasmid using Hieff Trans™
583 Liposomal Transfection Reagent, following the manufacturer's instructions. Cells
584 transfected with the empty vector pEGFP-N1 were used as controls. At 36 hpt, cells
585 were collected for CUT&Tag analysis. For the CUT&Tag, cells were fixed with 1%
586 formaldehyde at room temperature for 10 min, and the reaction was quenched with
587 0.125 M glycine. After centrifugation, cells were permeabilized using ice-cold wash
588 buffer containing 0.05% digitonin. Primary antibody incubation was carried out
589 overnight at 4 °C using mouse anti-GFP antibody (1:1000), followed by a 2 h incubation
590 at room temperature with Protein A/G-conjugated secondary antibody (1:100). Cells
591 were then incubated at 37 °C for 1 h with a Protein A-Tn5 transposase complex (1:100)
592 preloaded with Illumina sequencing adapters.

593 The reaction was terminated using lysis buffer containing 10% SDS, followed by
594 proteinase K digestion. DNA was purified and amplified by PCR (12 cycles) using the
595 NEBNext Ultra II DNA Library Preparation Kit. Fragment size distribution (150-300 bp)
596 was confirmed using the Agilent 2100 Bioanalyzer. Sequencing was performed on the
597 Illumina NovaSeq 6000 platform, producing 150 bp paired-end reads. Raw reads were
598 quality-checked using FastQC and aligned to the human reference genome (hg38).
599 Peak calling was conducted using MACS2 (v2.2.7) with the parameters --nomodel --
600 qvalue 0.05. Genomic annotation, GO analysis, and *de novo* motif discovery were
601 performed using HOMER (v4.11). Identified motifs were matched to known
602 transcription factor binding motifs using TOMTOM, with a statistical significance

603 threshold of $p < 0.001$.

604 **Chromatin Immunoprecipitation (ChIP) assays**

605 ChIP assays were performed to validate the direct binding of MmpE to the promoter
606 regions of target genes. HEK293T cells were transfected with either EGFP, or MmpE-
607 EGFP expression plasmids. Cross-linking, chromatin isolation, fragmentation, and
608 immunoprecipitation were carried out following the same procedure described for the
609 CUT&Tag assay. DNA was purified from both input and immunoprecipitated (IP)
610 samples and subjected to PCR using primers specific to the promoter regions of the
611 target genes (-100 bp to +50 bp relative to the transcription start site). *GAPDH* primers
612 were used as a negative control. PCR products were analyzed by agarose gel
613 electrophoresis. For quantitative analysis, ChIP-qPCR was carried out using the same
614 primer sets. All reactions were performed in triplicate. Relative enrichment was
615 calculated using the $2^{-\Delta Ct}$ method with normalization to input DNA.

616 **Electrophoretic mobility shift assays (EMSA)**

617 DNA substrates were amplified by PCR from the genomic DNA of *Mycobacterium*
618 *tuberculosis* H37Rv. The sequences of the oligonucleotide fragments used in the assay
619 are listed in Table S7. EMSA was carried out using a modified protocol as previously
620 described (Li *et al.,* 2020). Each 20 μL reaction contained PCR-amplified DNA
621 fragments, purified MmpE protein at varying concentrations, and binding buffer
622 composed of 20mM Tris-HCl (pH 8.0), 50mM KCl, 50mM $MgCl_2$, 0.2 mM $NiSO_4$,
623 0.05 mg/mL bovine serum albumin (BSA), 1mM DTT, 10% (v/v) glycerol. Reaction
624 mixtures were incubated on ice for 30 minutes to allow protein-DNA complex formation.
625 Samples were then resolved on a 4.8% native polyacrylamide gel using a running
626 buffer containing 15 mM Tris-HCl (pH 7.5), 0.1 M glycine, 1mM DTT, 50 μM $MgCl_2$ and
627 0.2 μM $NiSO_4$ at 80 V. Following electrophoresis, gels were stained with ethidium
628 bromide and visualized using a Gel Imaging Analysis System (JIAPENG, China).

629 **Detection of Phagosomal Acidification**

630 THP-1 cells were seeded at 70% confluency in poly-L-lysine-coated 35-mm glass-

631 bottom dishes and maintained in RPMI 1640 supplemented with 10% (v/v) FBS and
632 200 nM PMA for 24 h at 37 °C under 5% CO_2. After two washes with PBS, the cells
633 were infected with DiD-labeled BCG strains at a MOI of 10 for 24 h, LysoTracker was
634 added for 1 h, followed by Hoechst staining for 15 minutes to visualize the nuclei.
635 Hoechst staining was excited at 350 nm and emitted at 461 nm (blue), while
636 LysoTracker was excited at 504 nm and emitted at 511 nm (green); DiD was excited
637 at 644 nm and emitted at 665 nm (red). Image analysis was performed by calculating
638 the percentage co-localization of LysoTracker with the phagosomes to assess the
639 effects of different mutants.

640 **Colony-Forming Unit (CFU) assay**

641 For bacterial preparation, mid-log phase cultures of BCG (OD_{600} = 0.6) were harvested,
642 washed with PBS, and resuspended in fresh medium. THP-1 cells were seeded in 12-
643 well plates at a density of 5×10^5 cells per well and and differentiated into macrophage-
644 like cells by treatment with 100 nM PMA for 24 h. After differentiation, cells were
645 washed with PBS and treated with the PI3K-Akt-mTOR pathway inhibitor BEZ235 at
646 various concentrations (0-200 nM). BEZ235 was applied with bacterial infection (co-
647 treatment). An equivalent volume of DMSO was used as a vehicle control for all
648 treatment conditions.
649 Cells were infected at a MOI of 10:1 and incubated for 4 h. After infection, extracellular
650 bacteria were removed by treatment with penicillin-streptomycin (100 μg/mL) for 4 h.
651 Cells were then washed three times with PBS and maintained in antibiotic-free medium
652 until harvest. Intracellular bacterial burdens were assessed at multiple time points post-
653 infection, macrophages were lysed with 0.25% SDS for 10 minutes at room
654 temperature. Lysates were serially diluted in PBS, and 100 μL aliquots of each dilution
655 were plated on Middlebrook 7H10 agar supplemented with 10% OADC and kanamycin
656 (50 μg/mL). Plates were incubated at 37 °C for 14 days. CFUs were enumerated, and
657 final counts were calculated by applying the corresponding dilution factors. BCG
658 strains used in this study are listed in Table S6.

659 **Mice infection**

660 Mice were infected as described previously (Chen *et al.,* 2022), with minor
661 modifications. Mid-log phase BCG cultures were washed twice in PBS containing 0.05%
662 Tween 80 and briefly sonicated to disrupt bacterial clumps. Female C57BL/6 mice were
663 anesthetized with isoflurane and intranasally inoculated with 1×10^7 CFUs of BCG in
664 40 μL of PBS. To confirm the inoculation dose, six mice were euthanized at 48 hpi.
665 Lungs were harvested, homogenized in 1 mL of PBS using a tissue homogenizer, and
666 serial dilutions of the homogenates were plated on Middlebrook 7H10 agar
667 supplemented with 10% OADC. Plates were incubated at 37 °C with 5% CO_2 for
668 14 days, after which CFUs were enumerated.

669 **Histological analysis**

670 Lung tissues from BCG-infected mice were fixed in 4% phosphate-buffered formalin at
671 room temperature for 24 h, followed by paraffin embedding. Paraffin-embedded tissue
672 samples were sectioned into 2-3 μm thick slices using a microtome. Sections were
673 deparaffinized, rehydrated through a graded ethanol series, and stained with
674 hematoxylin and eosin (H&E). Stained tissue sections were examined using an
675 Olympus BX53 light microscope. For digital analysis and annotation, scanned slides
676 were visualized using CaseViewer software (version 2.0; 3DHISTECH).

677 **Ethics approval**

678 All animal experiments were conducted in accordance with the protocols approved by
679 the Animal Ethics Committee of the Huazhong Agricultural University.

680 **Statistical analyses**

681 Data are presented as mean ± standard deviation (SD). Statistical comparisons were
682 performed using two-tailed unpaired Student's *t*-tests or two-way ANOVA. A *P*-value
683 of less than 0.05 was considered significant, with significance levels indicated as
684 follows: $P < 0.05$ (*), $P < 0.01$ (**), and $P < 0.001$ (***). All statistical analyses were
685 performed using GraphPad Prism (version 8.0). Data were obtained from at least three
686 independent biological replicates, each including two or more technical replicates.

687 **Acknowledgments**

This work was supported by the Fundamental Research Funds for the Central Universities (#2662023DKQD001), Talent Start-up Funds of Huazhong Agricultural University (#11042310008), National Natural Science Foundation of China (#32473123), China Agriculture Research System of MOF and MARA (#CARS-37), and National Key Research and Development Program of China (#2021YFD1800403).

Author contributions

Conceptualization: L. C., A. G., and L. Z.; Methodology: L. C.; Validation: L. C., B. D., and Q. J.; Formal analysis: L. C., Y. W.; Investigation: L. C., B. D., Q. J., and Y. W.; Resources: A. G., L. Z., and Y. C.; Data curation: L. C., Q. J., and Y. W.; Writing - original draft: L. C., L. Z., and A. G.; Writing - review & editing: L. C., L. Z., and A. G.; Visualization: L. C., Q. J., Y. C., L. Z., and A. G.; Supervision: A. G., and L. Z.; Project administration: A. G., and L. Z.; Funding acquisition: A. G., L. Z., and Y. C.

Disclosure and competing interest statement

The authors declare no competing interests.

References

Agarwal S, Agarwal S, Jin H, Pancholi P, Pancholi V (2012) **Serine/threonine phosphatase (SP-STP), secreted from Streptococcus pyogenes, is a pro-apoptotic protein** *J Biol Chem* **287**:9147-67.

Aggeletopoulou I, Thomopoulos K, Mouzaki A, Triantos C (2022) **Vitamin D-VDR novel anti-inflammatory molecules-new insights into their effects on liver diseases** *Int J Mol Sci* **23**:8465.

Alsayed SSR, Gunosewoyo H (2024) **Combating Tuberculosis via restoring the host immune capacity by targeting Mtb kinases and phosphatases** *Int J Mol Sci* **25**:12481.

Baruch K, Gur-Arie L, Nadler C, Koby S, Yerushalmi G, Ben-Neriah Y, Yogev O, Shaulian E, Guttman C, Zarivach R, Rosenshine I (2011) **Metalloprotease type III effectors that specifically cleave JNK and NF-κB** *EMBO J* **30**:221-31.

715 Bhadouria J, Giri J (2022) **Purple acid phosphatases: roles in phosphate utilization**
716 **and new emerging functions** *Plant Cell Rep* **41**:33-51.

717 Bhadouria J, Singh AP, Mehra P, Verma L, Srivastawa R, Parida SK, Giri J (2017)
718 **Identification of purple acid phosphatases in chickpea and potential roles of**
719 **CaPAP7 in seed phytate accumulation** *Sci Rep* **7**:11012.

720 Bierne H, Cossart P (2021) **When bacteria target the nucleus: the emerging family**
721 **of nucleomodulins** *Cell Microbiol* **14**:622-33.

722 Buchanan G, Sargent F, Berks BC, Palmer T (2001) **A genetic screen for**
723 **suppressors of *Escherichia coli* Tat signal peptide mutations establishes a**
724 **critical role for the second arginine within the twin-arginine motif** *Arch Microbiol*
725 **177**:107-12.

726 Cautain B, Hill R, de Pedro N, Link W (2015) **Components and regulation of nuclear**
727 **transport processes** *FEBS J* **282**:445-62.

728 Chai Q, Wang L, Liu CH, Ge B (2020) **New insights into the evasion of host innate**
729 **immunity by *Mycobacterium tuberculosis*** *Cell Mol Immunol* **17**:901-913.

730 Chandra P, Grigsby SJ, Philips JA (2022) **Immune evasion and provocation by**
731 ***Mycobacterium tuberculosis*** *Nat Rev Microbiol* **20**:750-766.

732 Chen L, Duan B, Chen P, Jiang Q, Wang Y, Lu L, Chen Y, Hu C, Zhang L, Guo A (2025)
733 **A conserved mycobacterial nucleomodulin hijacks the host COMPASS complex**
734 **to reprogram pro-inflammatory transcription and promote intracellular survival**
735 *eLife* **14**:RP107677

736 Chen L, Li X, Xu P, He ZG (2022) **A novel zinc exporter CtpG enhances resistance**
737 **to zinc toxicity and survival in *Mycobacterium bovis*** *Microbiol Spectr* 10:e0145621.

738 Chen Y, Du J, Zhang Z, Liu T, Shi Y, Ge X, Li YC (2014) **MicroRNA-346 mediates**
739 **tumor necrosis factor α-induced downregulation of gut epithelial vitamin D**
740 **receptor in inflammatory bowel diseases** *Inflamm Bowel Dis* **20**:1910-8.

741 Comba S, Menendez-Bravo S, Arabolaza A, Gramajo H (2013) **Identification and**
742 **physiological characterization of phosphatidic acid phosphatase enzymes**
743 **involved in triacylglycerol biosynthesis in *Streptomyces coelicolor*** *Microb Cell*
744 *Fact* **12**:9.

745 Dean P, Scott JA, Knox AA, Quitard S, Watkins NJ, Kenny B (2010) **The**
746 **enteropathogenic *E. coli* effector EspF targets and disrupts the nucleolus by a**
747 **process regulated by mitochondrial dysfunction** *PLoS Pathog* **6**:e1000961.

748 Evans SM, Rodino KG, Adcox HE, Carlyon JA (2018) ***Orientia tsutsugamushi* uses**
749 **two Ank effectors to modulate NF-κB p65 nuclear transport and inhibit NF-κB**
750 **transcriptional activation** *PLoS Pathog* **14**:e1007023.

751 Fang J, Dong C, Xiong S (2022) ***Mycobacterium tuberculosis* Rv0790c inhibits the**
752 **cellular autophagy at its early stage and facilitates mycobacterial survival** *Front*
753 *Cell Infect Microbiol* **12**:1014897.

754 Fang S, Wan X, Zou X, Sun S, Hao X, Liang C, Zhang Z, Zhang F, Sun B, Li H, Yu B
755 (2021) **Arsenic trioxide induces macrophage autophagy and atheroprotection by**
756 **regulating ROS-dependent TFEB nuclear translocation and AKT/mTOR pathway**
757 *Cell Death Dis* **12**:88.

758 Feder D, McGeary RP, Mitić N, Lonhienne T, Furtado A, Schulz BL, Henry RJ, Schmidt
759 S, Guddat LW, Schenk G (2020) **Structural elements that modulate the substrate**
760 **specificity of plant purple acid phosphatases: Avenues for improved**
761 **phosphorus acquisition in crops** *Plant Sci* **294**:110445.

762 Fontes MR, Teh T, Kobe B (2000) **Structural basis of recognition of monopartite**
763 **and bipartite nuclear localization sequences by mammalian importin-alpha** *J Mol*
764 *Biol* **297**:1183-94.

765 Forrellad MA, Blanco FC, Marrero Diaz de Villegas R, Vázquez CL, Yaneff A, García
766 EA, Gutierrez MG, Durán R, Villarino A, Bigi F (2020) **Rv2577 of *Mycobacterium***

767 ***tuberculosis* Is a virulence factor with dual phosphatase and phosphodiesterase**
768 **functions** *Front Microbiol* **11**:570794.

769 Ge P, Lei Z, Yu Y, Lu Z, Qiang L, Chai Q, Zhang Y, Zhao D, Li B, Pang Y, Liu CH, Wang
770 J (2022) ***M. tuberculosis* PknG manipulates host autophagy flux to promote**
771 **pathogen intracellular survival** *Autophagy* **18**:576-594.

772 Gounis M, Hamidi H, Ivaska J (2025) **mTORC1 shutdown unleashes TFEB to drive**
773 **triple-negative breast cancer invasion** *Dev Cell* **60**:979-981.

774 Hanford HE, Von Dwingelo J, Abu Kwaik Y (2021) **Bacterial nucleomodulins: a**
775 **coevolutionary adaptation to the eukaryotic command center** *PLoS Pathog*
776 **17**:e1009184.

777 Hodgson A, Wier EM, Fu K, Sun X, Yu H, Zheng W, Sham HP, Johnson K, Bailey S,
778 Vallance BA, Wan F (2015) **Metalloprotease NleC suppresses host NF-**
779 **κB/inflammatory responses by cleaving p65 and interfering with the p65/RPS3**
780 **interaction** *PLoS Pathog* **11**:e1004705.

781 Hsu CM, Lin PM, Tsai YT, Tsai MS, Tseng CH, Lin SF, Yang MY (2018) **NVP-BEZ235,**
782 **a dual PI3K-mTOR inhibitor, suppresses the growth of FaDu hypopharyngeal**
783 **squamous cell carcinoma and has a synergistic effect with Cisplatin** *Cell Death*
784 *Discov* **4**:57.

785 Jeong SJ, Stitham J, Evans TD, Zhang X, Rodriguez-Velez A, Yeh YS, Tao J,
786 Takabatake K, Epelman S, Lodhi IJ, Schilling JD, DeBosch BJ, Diwan A, Razani B
787 (2021) **Trehalose causes low-grade lysosomal stress to activate TFEB and the**
788 **autophagy-lysosome biogenesis response**. Autophagy **17**:3740-3752.

789 Jermy A (2010) **Chlamydia gets a NUE look** *Nat Rev Microbiol*. **8**:614.

790 Jose L, Ramachandran R, Bhagavat R, Gomez RL, Chandran A, Raghunandanan S,
791 Omkumar RV, Chandra N, Mundayoor S, Kumar RA (2016) **Hypothetical protein**
792 **Rv3423.1 of *Mycobacterium tuberculosis* is a histone acetyltransferase** *FEBS J*
793 **283**:265-81.

794 Kosugi S, Hasebe M, Matsumura N, Takashima H, Miyamoto-Sato E, Tomita M,
795 Yanagawa H (2009) **Six classes of nuclear localization signal specific to different**
796 **binding grooves of importin alpha** *J Biol Chem* **284**:478-485.

797 Lebreton A, Job V, Ragon M, Le Monnier A, Dessen A, Cossart P, Bierne H (2014)
798 **Structural basis for the inhibition of the chromatin repressor BAHD1 by the**
799 **bacterial nucleomodulin LntA** *mBio* **5**: e00775-13.

800 Lebreton A, Lakisic G, Job V, Fritsch L, Tham TN, Camejo A, Matteï PJ, Regnault B,
801 Nahori MA, Cabanes D, Gautreau A, Ait-Si-Ali S, Dessen A, Cossart P, Bierne H (2011)
802 **A bacterial protein targets the BAHD1 chromatin complex to stimulate type III**
803 **interferon response** *Science* **331**:1319-21.

804 Li T, Lu Q, Wang G, Xu H, Huang H, Cai T, Kan B, Ge J, Shao F (2013) **SET-domain**
805 **bacterial effectors target heterochromatin protein 1 to activate host rDNA**
806 **transcription** *EMBO Rep* **14**:733-40.

807 Li X, Chen L, Liao J, Hui J, Li W, He ZG (2020) **A novel stress-inducible CmtR-ESX3-**
808 **Zn^{2+} regulatory pathway essential for survival of *Mycobacterium bovis* under**
809 **oxidative stress** *J Biol Chem* **295**:17083-17099.

810 Li X, Zhang M, Zhou G, Xie Z, Wang Y, Han J, Li L, Wu Q, Zhang S (2023) **Role of**
811 **Rho GTPases in inflammatory bowel disease** *Cell Death Discov* **9**:24.

812 Liu PT, Stenger S, Li H, Wenzel L, Tan BH, Krutzik SR, Ochoa MT, Schauber J, Wu K,
813 Meinken C, Kamen DL, Wagner M, Bals R, Steinmeyer A, Zügel U, Gallo RL,
814 Eisenberg D, Hewison M, Hollis BW, Adams JS, Bloom BR, Modlin RL (2006) **Toll-like**
815 **receptor triggering of a vitamin D-mediated human antimicrobial response**
816 *Science* **311**:1770-3.

817 Liu SF, Yi ZC, Huang ZQ, Yuan ZD, Yang YC, Zhao Y, He QY, Yang WD, Li HY, Lin
818 CSK, Wang X (2025) **Enhanced biodegradation of glyphosate by *Chlorella***
819 ***sorokiniana* engineered with exogenous purple acid phosphatase** *Water Res*
820 **268**:122737.

821 Ma S, Ming Y, Wu J, Cui G (2024) **Cellular metabolism regulates the differentiation**
822 **and function of T-cell subsets** *Cell Mol Immunol* **21**:419-435.

823 Mitra S, Dunphy PS, Das S, Zhu B, Luo T, McBride JW (2018) ***Ehrlichia chaffeensis***
824 **TRP120 effector targets and recruits host polycomb group proteins for**
825 **degradation to promote intracellular infection** *Infect Immun* **86**:e00845-17.

826 Nasiri MJ, Venketaraman V (2025) **Advances in host-pathogen interactions in**
827 **Tuberculosis: emerging strategies for therapeutic intervention** *Int J Mol Sci*
828 **26**:1621.

829 Nisa A, Kipper FC, Panigrahy D, Tiwari S, Kupz A, Subbian S (2022) **Different**
830 **modalities of host cell death and their impact on *Mycobacterium tuberculosis***
831 **infection** *Am J Physiol Cell Physiol* **323**:C1444-C1474.

832 Pennini ME, Perrinet S, Dautry-Varsat A, Subtil A (2010) **Histone methylation by NUE,**
833 **a novel nuclear effector of the intracellular pathogen *Chlamydia trachomatis***
834 *PLoS Pathog* **6**:e1000995.

835 Rodriguez F, Lillington J, Johnson S, Timmel CR, Lea SM, Berks BC (2014) **Crystal**
836 **structure of the *Bacillus subtilis* phosphodiesterase PhoD reveals an iron and**
837 **calcium-containing active site** *J Biol Chem* **289**:30889-99.

838 Rolando M, Sanulli S, Rusniok C, Gomez-Valero L, Bertholet C, Sahr T, Margueron R,
839 Buchrieser C (2013) ***Legionella pneumophila* effector RomA uniquely modifies**
840 **host chromatin to repress gene expression and promote intracellular bacterial**
841 **replication** *Cell Host Microbe* **13**:395-405.

842 Schenk G, Guddat LW, Ge Y, Carrington LE, Hume DA, Hamilton S, de Jersey J (2000)
843 **Identification of mammalian-like purple acid phosphatases in a wide range of**
844 **plants** *Gene* **250**:117-25.

845 Sha S, Shi Y, Tang Y, Jia L, Han X, Liu Y, Li X, Ma Y (2021) ***Mycobacterium***
846 ***tuberculosis* Rv1987 protein induces M2 polarization of macrophages through**
847 **activating the PI3K/Akt1/mTOR signaling pathway** *Immunol Cell Biol* **99**:570-585.

848 Shaban L, Nguyen GT, Mecsas-Faxon BD, Swanson KD, Tan S, Mecsas J (2020)
849 ***Yersinia pseudotuberculosis* YopH targets SKAP2-dependent and independent**
850 **signaling pathways to block neutrophil antimicrobial mechanisms during**
851 **infection** *PLoS Pathog* **16**:e1008576.

852 Singh AP, Sharma S, Pagarware K, Siraji RA, Ansari I, Mandal A, Walling P, Aijaz S
853 (2018) **Enteropathogenic *E. coli* effectors EspF and Map independently disrupt**
854 **tight junctions through distinct mechanisms involving transcriptional and post-**
855 **transcriptional regulation** *Sci Rep* **8**:3719.

856 Singh PR, Dadireddy V, Udupa S, Kalladi SM, Shee S, Khosla S, Rajmani RS, Singh
857 A, Ramakumar S, Nagaraja V (2023) **The *Mycobacterium tuberculosis***
858 **methyltransferase Rv2067c manipulates host epigenetic programming to**
859 **promote its own survival** *Nat Commun* **14**:8497.

860 Singh PR, Nagaraja V (2025) **Epigenetic maneuvering: an emerging strategy for**
861 **mycobacterial intracellular survival** *Trends Microbiol* **33**:354-369.

862 Stanley NR, Palmer T, Berks BC (2000) **The twin arginine consensus motif of Tat**
863 **signal peptides is involved in Sec-independent protein targeting in *Escherichia***
864 ***coli*** *J Biol Chem* **275**:11591-6.

865 Steiert B, Weber MM (2025) **Nuclear warfare: pathogen manipulation of the**
866 **nuclear pore complex and nuclear functions** *mBio* **16**:e0194024.

867 Tang D, Chen M, Huang X, Zhang G, Zeng L, Zhang G, Wu S, Wang Y (2023) **SRplot:**
868 **A free online platform for data visualization and graphing** *PLoS One* **18**:e0294236.

869 Tian J, Zhu Y, Rao M, Cai Y, Lu Z, Zou D, Peng X, Ying P, Zhang M, Niu S, Li Y, Zhong
870 R, Chang J, Miao X (2020) **N^6-methyladenosine mRNA methylation**
871 **of PIK3CB regulates AKT signalling to promote PTEN-deficient pancreatic**
872 **cancer progression** *Gut* **69**:2180-2192.

873 Usategui-Martín R, De Luis-Román DA, Fernández-Gómez JM, Ruiz-Mambrilla M,
874 Pérez-Castrillón JL (2022) **Vitamin D receptor (VDR) gene polymorphisms modify**

875 **the response to vitamin d supplementation: a systematic review and meta-**
876 **analysis** *Nutrients* **14**:360.

877 Wang B, Martini-Stoica H, Qi C, Lu TC, Wang S, Xiong W, Qi Y, Xu Y, Sardiello M, Li
878 H, Zheng H (2024) **TFEB-vacuolar ATPase signaling regulates lysosomal function**
879 **and microglial activation in tauopathy** *Nat Neurosci* **27**:48-62.

880 Wang J, Ge P, Qiang L, Tian F, Zhao D, Chai Q, Zhu M, Zhou R, Meng G, Iwakura Y,
881 Gao GF, Liu CH (2017) **The mycobacterial phosphatase PtpA regulates the**
882 **expression of host genes and promotes cell proliferation** *Nat Commun* **8**:244.

883 Wong D, Bach H, Sun J, Hmama Z, Av-Gay Y (2011) ***Mycobacterium tuberculosis***
884 **protein tyrosine phosphatase (PtpA) excludes host vacuolar-H^+-ATPase to**
885 **inhibit phagosome acidification** *Proc Natl Acad Sci U S A* **108**:19371-6.

886 Yang H, Zhang H, Li Y, Xiang L, Liu J (2019) **BCG stimulation promotes dendritic**
887 **cell proliferation and expression of VDR and CYP27B1 in vitamin D-deficient**
888 **mice** *Mol Med Rep* **20**:5265-5271.

889 Yang L, Shi P, Zhao G, Xu J, Peng W, Zhang J, Zhang G, Wang X, Dong Z, Chen F,
890 Cui H (2020) **Targeting cancer stem cell pathways for cancer therapy** *Signal*
891 *Transduct Target Ther* **5**:8.

892 Yeung SL, Cheng C, Lui TK, Tsang JS, Chan WT, Lim BL (2009) **Purple acid**
893 **phosphatase-like sequences in prokaryotic genomes and the characterization of**
894 **an atypical purple alkaline phosphatase from *Burkholderia cenocepacia* J2315**
895 *Gene* **440**:1-8.

896 Zhang L, Kent JE, Whitaker M, Young DC, Herrmann D, Aleshin AE, Ko YH, Cingolani
897 G, Saad JS, Moody DB, Marassi FM, Ehrt S, Niederweis M (2022) **A periplasmic**
898 **cinched protein is required for siderophore secretion and virulence of**
899 ***Mycobacterium tuberculosis*** *Nat Commun* **13**:2255.

900 Zhang QA, Ma S, Li P, Xie J (2023) **The dynamics of *Mycobacterium tuberculosis***
901 **phagosome and the fate of infection** *Cell Signal* **108**:110715.

902 Zhang W, Dong C, Xiong S (2024) **Mycobacterial SapM hampers host autophagy**
903 **initiation for intracellular bacillary survival via dephosphorylating Raptor**
904 *iScience* **27**:109671.

905 Zheng R, Li Z, Fang W, Lou H, Liu F, Sun Q, Shi X, Liu H, Chen Q, Shen X, Yao L,
906 Guan L, Chen J, Xie Y, Yang Y, Yang H, Wang L, Qin L, Huang X, Wang J, Liu Z, Liu
907 H, Ge B, Xu J, Sha W (2025) **A genome-wide association study identified PRKCB**
908 **as a causal gene and therapeutic target for Mycobacterium avium complex**
909 **disease** *Cell Rep Med* **6**:101923.

910 Zhou Y, Dong B, Kim KH, Choi S, Sun Z, Wu N, Wu Y, Scott J, Moore DD (2020)
911 **Vitamin D Receptor Activation in Liver Macrophages Protects Against Hepatic**
912 **Endoplasmic Reticulum Stress in Mice** *Hepatology* **71**:1453-1466.

913 **Legends**

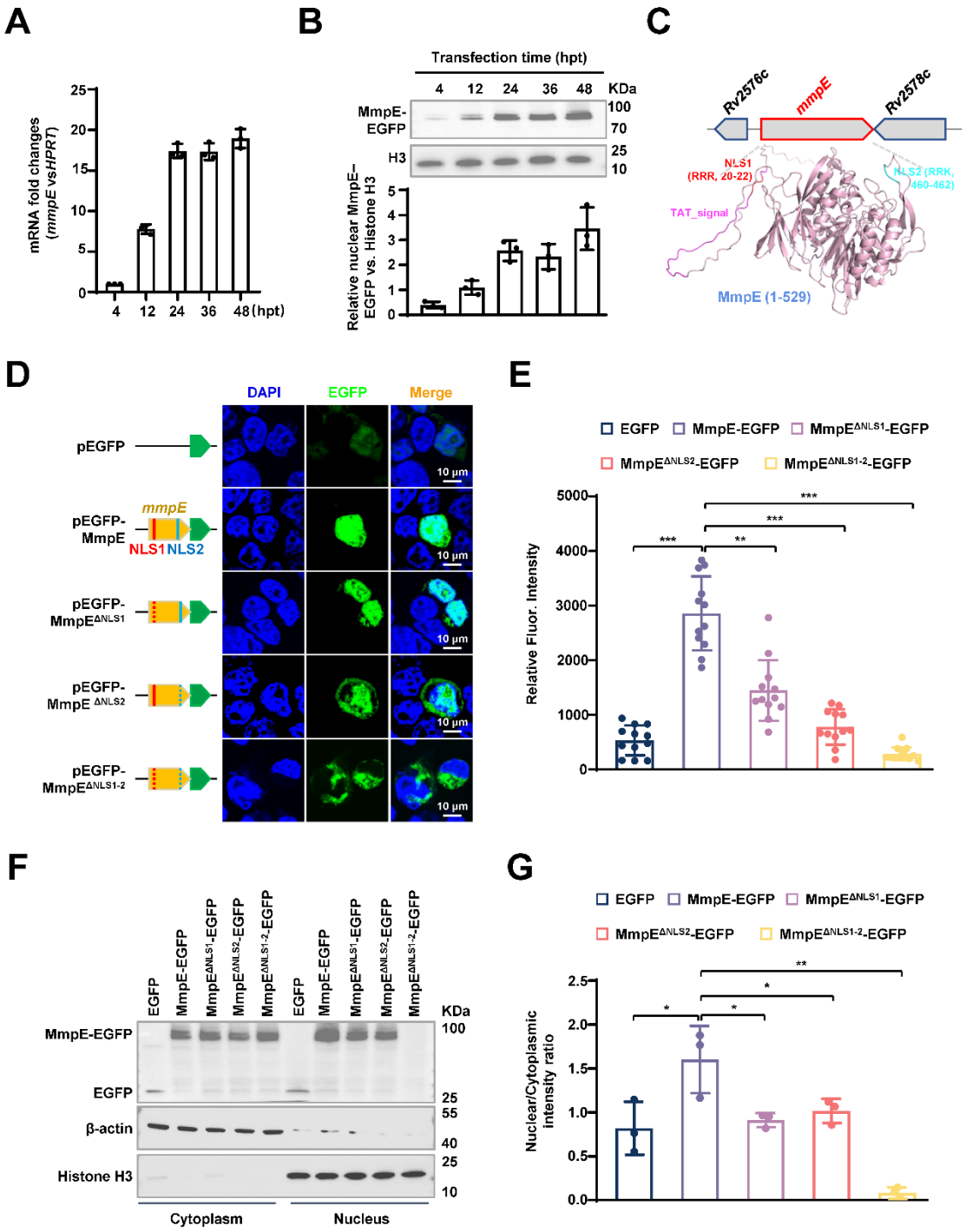

914

915 **Figure 1. NLSs are required for the nuclear translocation of MmpE.**

916 **(A)** qRT-PCR analysis of *mmpE* mRNA expression in HEK293T cells over 48 hpt. **(B)**
917 Western blot analysis of nuclear fractions showing time-dependent accumulation of
918 MmpE-EGFP (top), and corresponding quantification of nuclear MmpE-EGFP levels
919 (bottom). Histone H3 and β-actin were used as nuclear and cytoplasmic markers,
920 respectively. **(C)** Domain architecture of MmpE, including a Tat signal peptide (1-54

921 amino acids, with a twin-arginine translocation motif) and two nuclear localization
922 signals (NLS1: 20-22 aa; NLS2: 460-462 aa). The structure of the MmpE protein was
923 predicted using AlphaFold 2.2.0, with NLS1 and NLS2 highlighted in red and green,
924 respectively. **(D)** Subcellular localization of EGFP-tagged wild-type and NLS-deleted
925 MmpE. (left) Schematic representation of EGFP-tagged constructs. (right) Confocal
926 microscopy images of HEK293T cells transfected with the indicated constructs for 36
927 hpt. EGFP fluorescence (green) and nuclear staining with DAPI (blue) were visualized
928 using an FLUOVIEW software (v5.0). Scale bar, 10 μm. Images were acquired with a
929 ×100 oil immersion objective (NA = 1.4). **(E)** Quantification of nuclear EGFP intensity
930 of wild-type and mutant MmpE in (Figure **1D**). Data are shown as mean ± SD, n = 12
931 cells. **(F)** Western blot analysis of nuclear and cytoplasmic fractions from HEK293T
932 cells transfected with wild-type and mutant MmpE-EGFP confirmed their subcellular
933 localization. MmpE-EGFP was detected using an anti-GFP antibody, and histone H3
934 and β-actin served as nuclear and cytoplasmic markers, respectively. **(G)** Quantitative
935 analysis of MmpE-EGFP levels in the cytoplasmic and nuclear compartments of
936 (Figure **1F**). Data represent mean ± SD of three independent biological replicates.
937 Statistical significance determined using two-tailed unpaired Student's *t*-tests, $^{*}P <$
938 0.05, $^{**}P < 0.01$, $^{***}P < 0.001$.
939

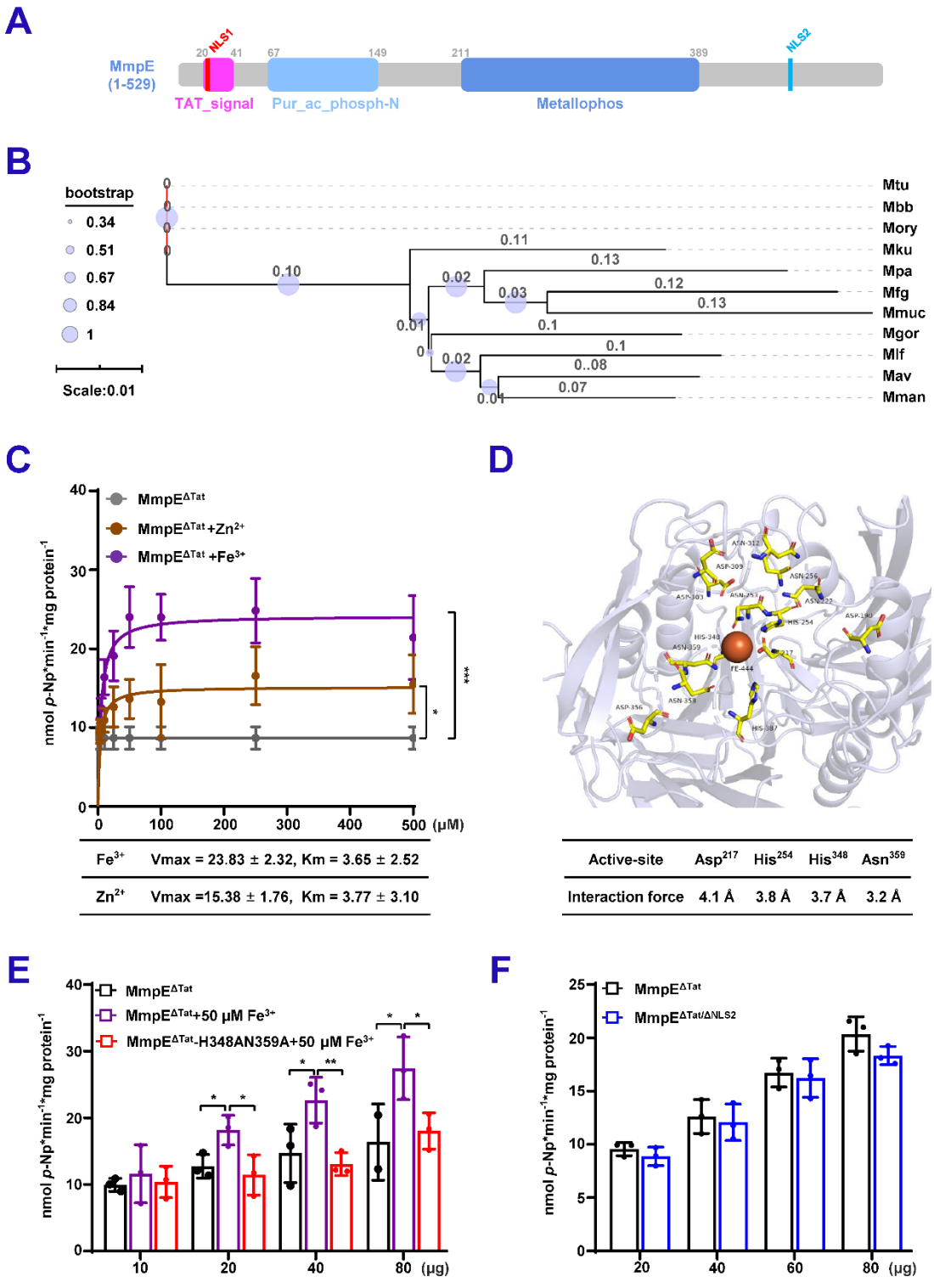

Figure 2. Deletion of NLSs does not alter the phosphatase activity of MmpE. (**A**) Domain architecture of MmpE. Schematic representation of MmpE with the annotated functional domains, including a Tat signal peptide (1-41 aa, twin-arginine translocation motif), a purple acid phosphatase domain (68-149 aa), a calcineurin-like phosphoesterase domain (211-389 aa) and two nuclear localization signals (NLS1: 20-

946 22 aa; NLS2: 460-462 aa). (**B**) Phylogenetic and structural conservation of MmpE.
947 Neighbor-joining phylogenetic tree of MmpE homologs across Mycobacterium species
948 (1,000 bootstrap replicates; values ≥50% shown). Species abbreviations: *M.*
949 *tuberculosis* (Mtu), *M. bovis* BCG (Mbb), *M. orygis* (Mory), *M. kubicae* (Mku), *M.*
950 *paraterrae* (Mpa), *M. farcinogenes* (Mfg), *M. mucogenicum* (Mmuc), *M. vicinigordonae*
951 (Mgor), *M. lentiflavum* (Mlf), *M. avium* (Mav), *M. manitobense* (Mman). **(C)**
952 Phosphatase activity of $MmpE^{\Delta Tat}$ (lacking the N-terminal Tat signal peptide) was
953 measured using *p*-NPP as the substrate in the presence of increasing concentrations
954 (0-500 μM) of Fe^{3+} and Zn^{2+}. **(D)** Prediction of metal ion-binding residues in MmpE.
955 Structural modeling and visualization were performed using PyMOL. Conserved
956 residues in the putative metal-binding pocket are shown as sticks, colored by atom
957 type. The predicted metal coordination site is highlighted, with key binding residues
958 labeled. Surface representation depicts the spatial accessibility of the pocket. (**E**)
959 Phosphatase activity of increasing concentrations of $MmpE^{\Delta Tat}$ and the mutant
960 $MmpE^{\Delta Tat}$-H348AN359A was measured in the absence or presence of 50 μM Fe^{3+}. (**F**)
961 Phosphatase activity of increasing concentrations of $MmpE^{\Delta Tat}$ and $MmpE^{\Delta Tat/\Delta NLS1-2}$
962 was measured under standard conditions. Data represent mean ± SD of three
963 independent biological replicates. Statistical significance determined using two-way
964 ANOVA, $^{*}P < 0.05$, $^{**}P < 0.01$, $^{***}P < 0.001$.

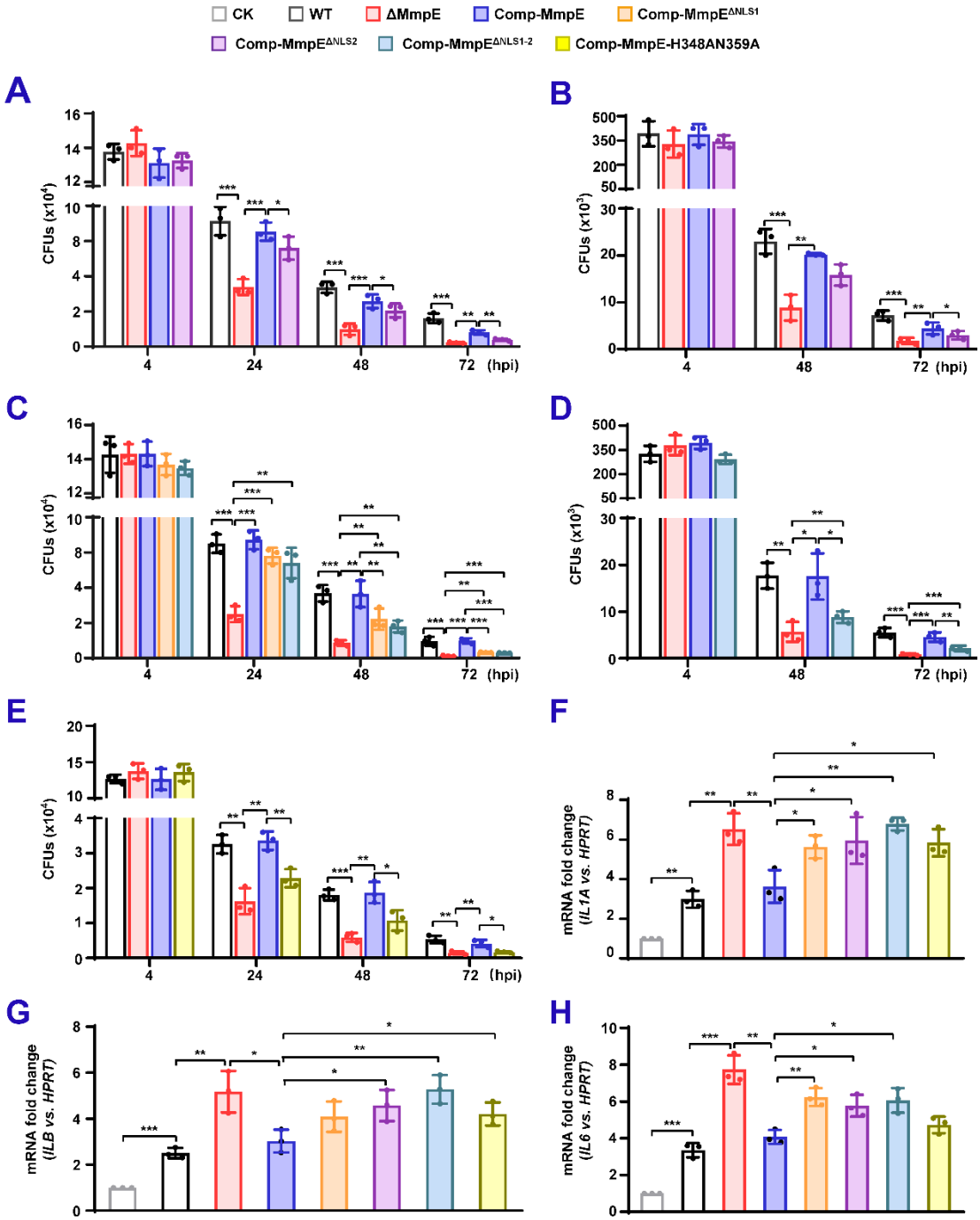

965

966 **Figure 3. The nuclear translocation and phosphatase activity of MmpE are**
967 **essential for *M. bovis* BCG survival in macrophage cells.**

968 **(A-B)** Intracellular survival of BCG strains in human THP-1 macrophages **(A)** and
969 RAW264.7 macrophages (**B**). Strains include BCG WT, ΔMmpE, Comp-MmpE, and
970 Comp-MmpE$^{\Delta NLS2}$. **(C-D)** Intracellular survival of strains in THP-1 (**C**) and RAW264.7
971 macrophages (**D**). Strains include BCG WT, ΔMmpE, Comp-MmpE, Comp-MmpE$^{\Delta NLS1}$
972 and Comp-MmpE$^{\Delta NLS1\text{-}2}$. **(E)** Intracellular survival of Comp-MmpE-H348AN359H

973 mutant in THP-1 cells. **(F-H)** Inflammatory cytokine expression in infected THP-1 cells.
974 mRNA levels of *IL-1A* (**F**), *IL-1B* (**G**), and *IL-6* (**H**) were quantified by qRT-PCR 24 hpi
975 with the indicated BCG strains. Data represent mean ± SD of three independent
976 biological replicates. Statistical significance determined using two-way ANOVA or two-
977 tailed unpaired Student's *t*-tests, *$P < 0.05$, **$P < 0.01$, ***$P < 0.001$.

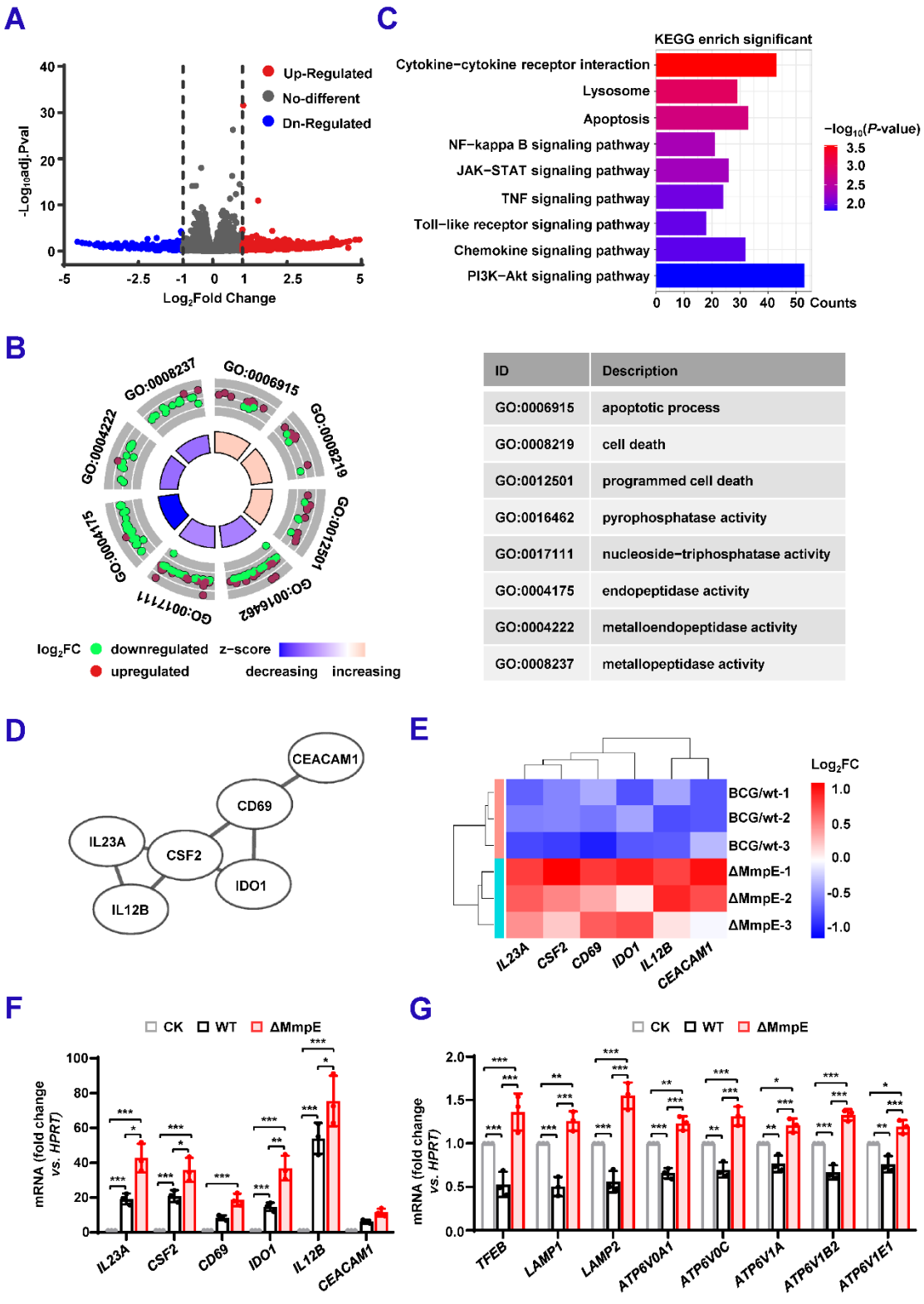

ID	Description
GO:0006915	apoptotic process
GO:0008219	cell death
GO:0012501	programmed cell death
GO:0016462	pyrophosphatase activity
GO:0017111	nucleoside−triphosphatase activity
GO:0004175	endopeptidase activity
GO:0004222	metalloendopeptidase activity
GO:0008237	metallopeptidase activity

Figure 4. MmpE regulates host transcription network involved in inflammation response and lysosomal maturation.

(A) Volcano plot showing DEGs in THP-1 cells infected with ΔMmpE versus WT strains. DEGs were defined as | $\log_2$(fold change) | ≥ 1 and $P < 0.05$. **(B)** Enrichment analysis

983 of DEGs shown in **(A)**. The circular plot shows enriched biological process and
984 molecular function terms. Outer rings represent GO terms (red) and downregulated
985 (green) genes; inner rings reflect z-scores (blue to pink). Selected terms are listed with
986 GO IDs and descriptions. **(C)** KEGG enrichment analysis of DEGs shown in **(A)**. Bar
987 length denotes the number of associated DEGs, and color represents statistical
988 significance ($-\log_{10}$ (*P*-value)). **(D)** Protein-protein interaction network of immune-
989 related DEGs, constructed using STRING v12.0 and visualized in Cytoscape. **(E)**
990 Heatmap of immune-related DEGs in ΔMmpE-infected and WT-infected THP-1 cells.
991 Log_2(fold change) values are shown across three biological replicates. Red and blue
992 indicate upregulation and downregulation, respectively. **(F-G)** qRT-PCR validation of
993 representative DEGs in THP-1 cells infected with WT or ΔMmpE for 24 hpi. Cytokine-
994 related genes (**F**); lysosomal acidification and V-ATPase subunits genes (**G**). Data
995 represent mean ± SD of three independent biological replicates. Statistical significance
996 determined using two-way ANOVA, $^{*}P < 0.05$, $^{**}P < 0.01$, $^{***}P < 0.001$.

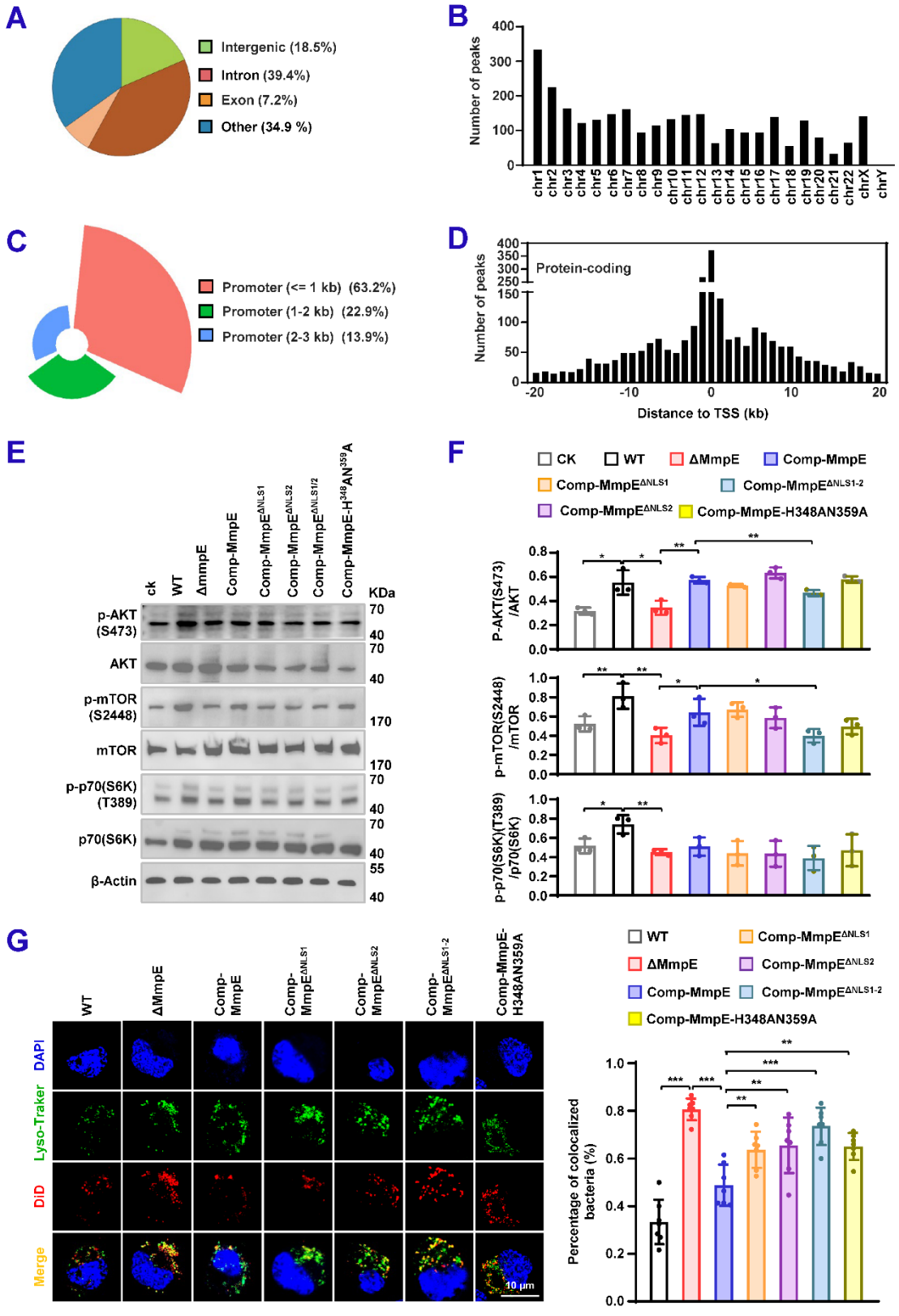

Figure 5. MmpE regulates the PI3K-Akt-mTOR signaling pathway during macrophage infection.

(A-D) Cut&Tag analysis of MmpE-binding regions in HEK293T cells. **(A)** Genomic distribution of potential MmpE-binding regions in HEK293T cells. **(B)** Chromosomal

1002 localization of MmpE-enriched peaks (fold enrichment > 9). **(C)** Biotype distribution of
1003 potential MmpE-binding regions in HEK293T cells. **(D)** Distribution of binding sites
1004 relative to the nearest transcription start sites (TSS) within ±20 kb of protein-coding
1005 genes. (**E**) Immunoblot analysis of pathway activation in THP-1 macrophages infected
1006 with WT, ΔMmpE, Comp-MmpE, Comp-MmpE$^{\Delta NLS1}$, Comp-MmpE$^{\Delta NLS2}$, Comp-
1007 MmpE$^{\Delta NLS1\text{-}2}$, or Comp-MmpE-H348A/N359A. Phosphorylation of Akt, mTOR, and
1008 p70S6K was evaluated at 8 hpi. **(F)** Quantification of phosphorylation levels across
1009 time points. **(G)** (left) Confocal microscopy analysis of phagosome acidification in
1010 infected THP-1 macrophages at 24 hpi. Cells were stained with LysoTracker Red and
1011 BCG strains were stained with DiD. (right) Co-localization between mycobacteria and
1012 LysoTracker was assessed. Representative images showing co-localization of
1013 intracellular bacterial with LysoTracker signal. Scale bar, 10 μm. Data represent mean
1014 ± SD of three independent biological replicates. Statistical significance determined
1015 using two-way ANOVA or two-tailed unpaired Student's *t*-tests, *$P < 0.05$, **$P < 0.01$,
1016 ***$P < 0.001$.

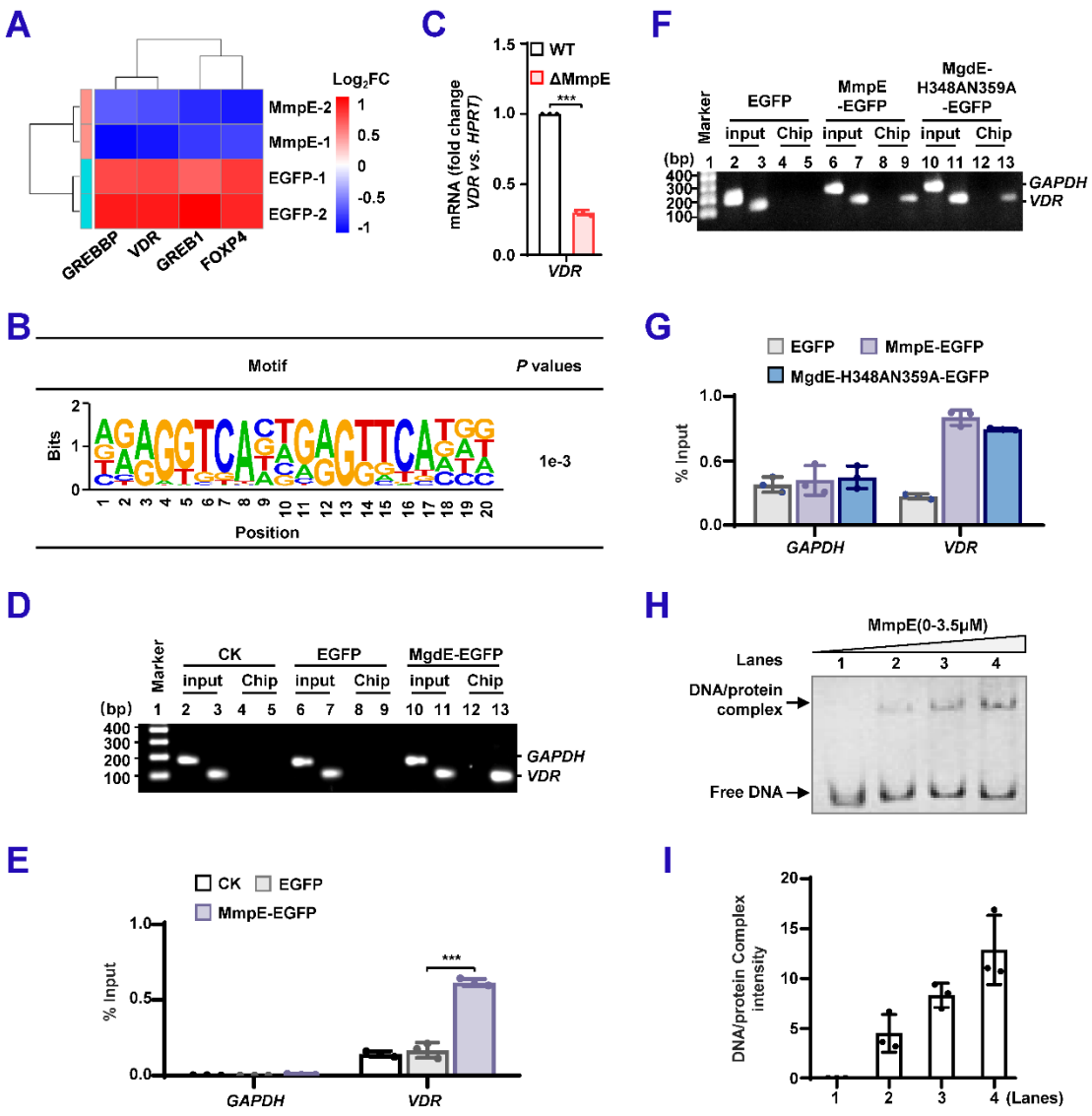

Figure 6. MmpE suppresses the expression of *VDR* during BCG infection

(A) Heatmap of transcription factors associated with MmpE ChIP-seq peaks in HEK293T cells. Color scale indicates expression changes (red: upregulated; blue: downregulated). **(B)** *De novo* motif analysis of MmpE-bound sequences using HOMER. Enrichment P-values were calculated with TOMTOM. "% of targets" indicates the proportion of peaks containing each motif; letter height reflects nucleotide frequency. **(C)** Quantitative RT-PCR analysis of VDR expression in THP-1 cells infected with WT or ΔMmpE strains for 24 h. **(D-G)** ChIP-PCR and qPCR analysis of the *VDR* promoter region. HEK293T cells were transfected with EGFP, MmpE-EGFP, or MmpE-H348A/N359A-EGFP. Chromatin was immunoprecipitated using anti-GFP antibody. PCR was performed with primers targeting the *VDR* promoter and GAPDH (negative

control), and products were analyzed by agarose electrophoresis (**D, F**). Enrichment was quantified by qPCR using the $2^{-\Delta Ct}$ method (**E, G**). **(H-I)** EMSA using purified MmpE protein and a DNA probe corresponding to the VDR promoter. Samples were resolved by native PAGE. Arrows indicate the positions of free DNA and slower-migrating species (**H**); signal intensities were quantified by densitometry (**I**). Data represent mean ± SD of three independent biological replicates. Statistical significance determined using two-way ANOVA or two-tailed unpaired Student's *t*-tests, ***$P < 0.001$.

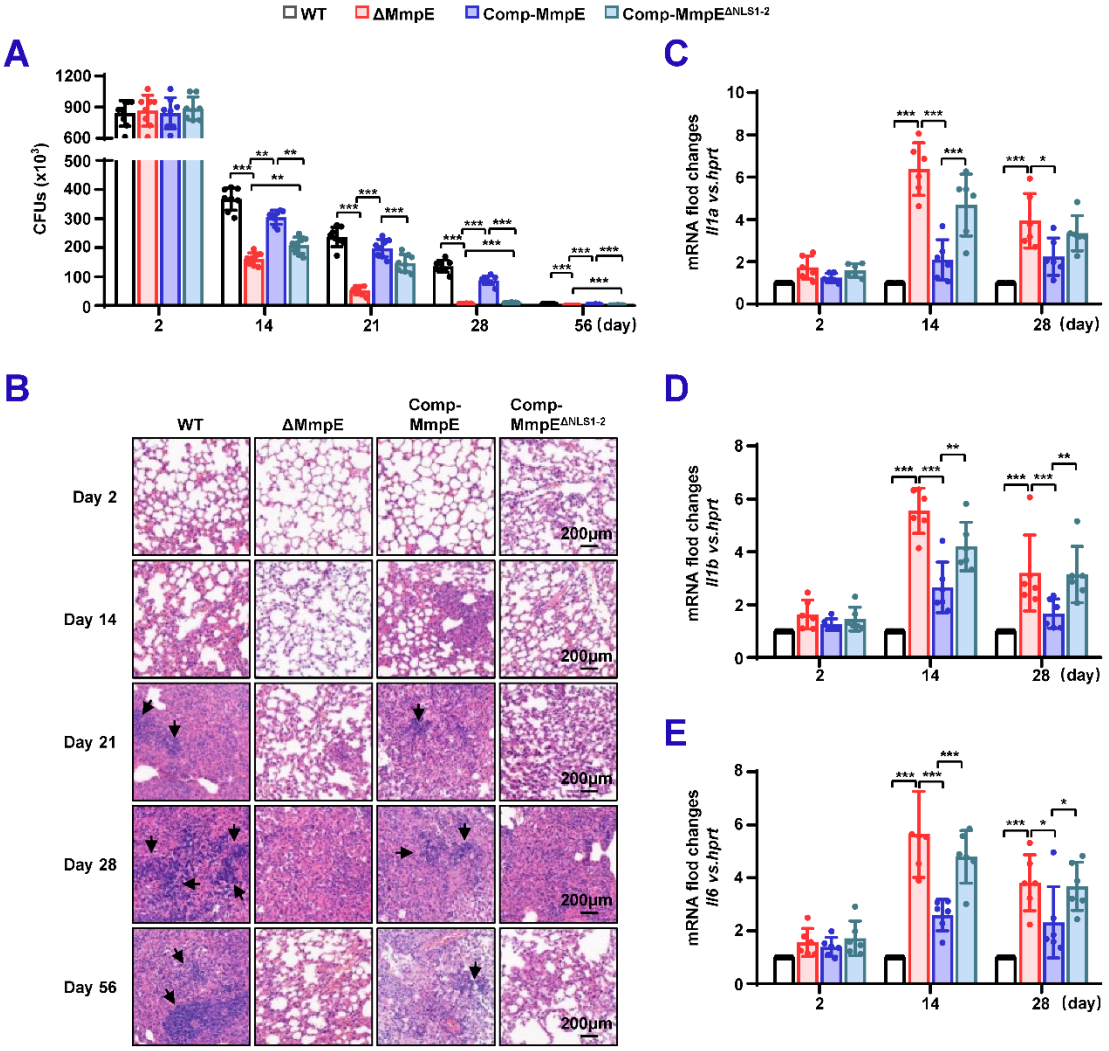

Figure 7. Nuclear translocation of MmpE is essential for mycobacterial survival in mice.

(**A**) Bacterial burden in lungs of infected mice. Specific pathogen-free (SPF) C57BL/6 mice (n = 6 per group) were intranasally infected with 1.0×10^7 CFUs of BCG strains, including WT, ΔMmpE, Comp-MmpE, or Comp-MmpE$^{\Delta NLS1\text{-}2}$. Bacterial titers in lung

homogenates were quantified by CFU assays at 0, 14, 28, and 56 dpi. **(B)** Histopathology of infected lung tissues. Hematoxylin and eosin (H&E)-stained lung sections from mice infected as in (**A**) show granulomatous inflammation, Scale bars: 200 μm. **(C-D)** Pro-inflammatory cytokine expression in the spleen of infected mice. qRT-PCR analysis of cytokine mRNA levels of *Il1a* (**C**), *Il1b* (**D**)and *Il6* (**E**) in spleen tissues from infected mice (n = 6/group) at 2 to 28 dpi. Data represent mean ± SD of three independent biological replicates. Statistical significance determined using two-way ANOVA, $^{*}P < 0.05$, $^{**}P < 0.01$, $^{***}P < 0.001$.

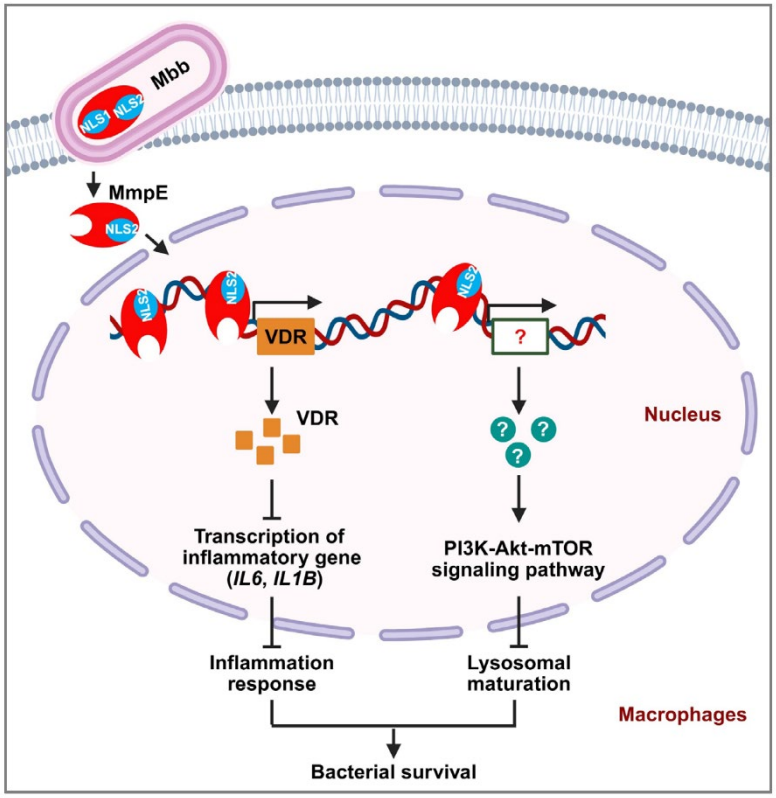

Figure 8. Schematic diagram of nucleomodulin MmpE-mediated immune suppression and enhanced mycobacterial survival.

During infection, the nucleomodulin MmpE translocates into the host nucleus via its C-terminal NLS2 motif (RRK$^{460\text{-}462}$), where it binds to the VDR promoter and suppresses transcription of inflammatory genes. Simultaneously, MmpE regulates the PI3K-Akt-mTOR signaling pathway, thereby inhibiting lysosome maturation. These dual mechanisms contribute to immune evasion and promote intracellular survival of mycobacteria.

1059 **Supplementary figures**

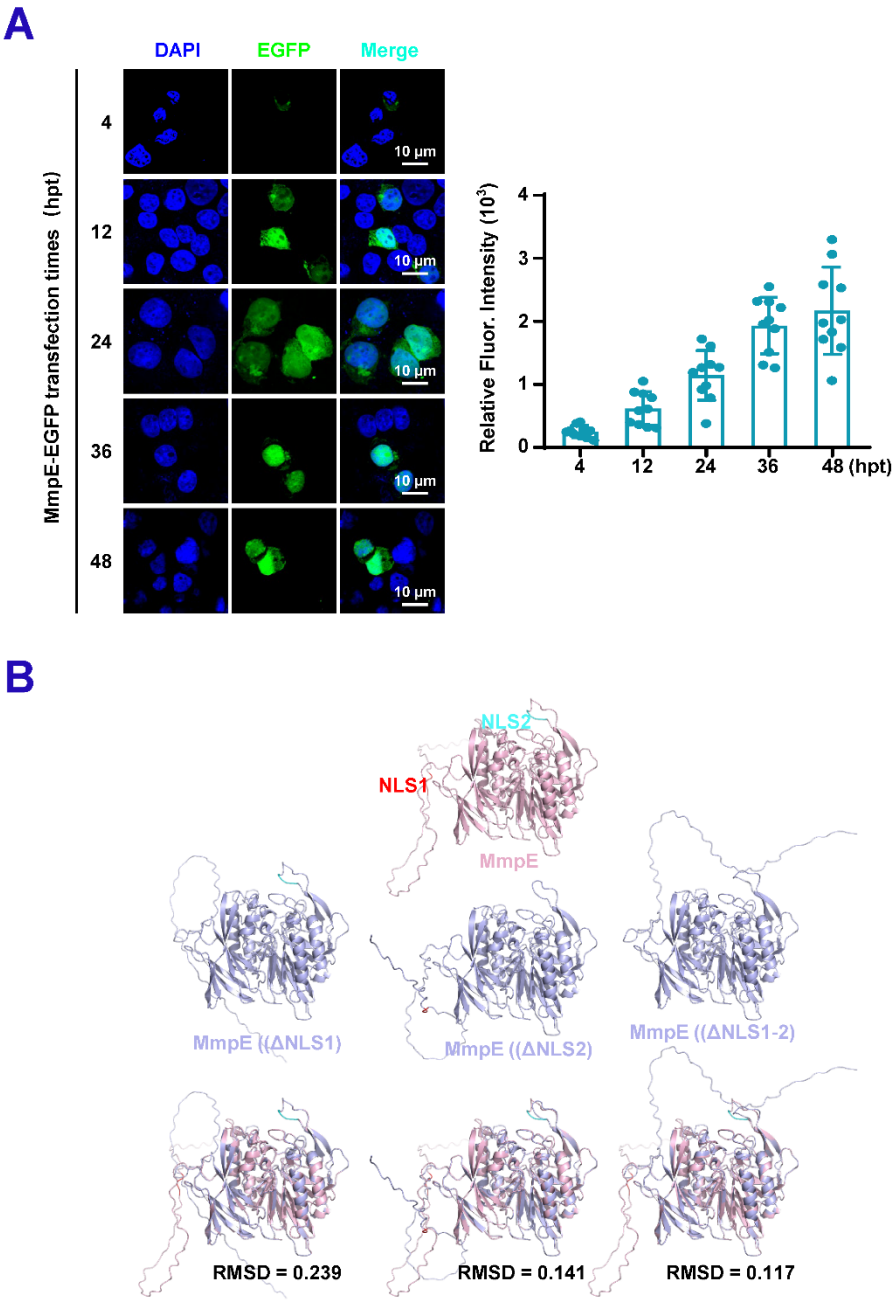
A
DAPI
EGFP
Merge
MmpE-EGFP transfection times (hpt)
4
12
24
36
48
10 μm
Relative Fluor. Intensity (10³)
0
1
2
3
4
4
12
24
36
48 (hpt)
B
NLS2
NLS1
MmpE
MmpE ((ΔNLS1)
MmpE ((ΔNLS2)
MmpE ((ΔNLS1-2)
RMSD = 0.239
RMSD = 0.141
RMSD = 0.117
C
BCG/MmpE-Flag
BCG/MmpEΔNLS1-Flag
BCG/MmpEΔNLS2-Flag
BCG/MmpEΔNLS1-2-Flag
BCG/MmpE-H348AN359A-Flag
BCG/MmpE-Flag
BCG/MmpEΔNLS1-Flag
BCG/MmpEΔNLS2-Flag
BCG/MmpEΔNLS1-2-Flag
BCG/MmpE-H348AN359A-Flag
KDa
MmpE-Flag
55
40
Ag85B
40
25
GlpX
55
35
Whole-cell lysate
Culture filtrate
D
CK
BCG/MmpE-Flag
BCG/MmpEΔNLS1-Flag
BCG/MmpEΔNLS2-Flag
BCG/MmpEΔNLS1-2-Flag
CK
BCG/MmpE-Flag
BCG/MmpEΔNLS1-Flag
BCG/MmpEΔNLS2-Flag
BCG/MmpEΔNLS1-2-Flag
KDa
MmpE-Flag
70
40
β-actin
55
40
Histone H3
25
10
Cytoplasm
Nucleus

1060

1061 **Supplementary Figure 1. Identification of MmpE as a nucleomodulin in**
1062 **Mycobacterium.**
1063 (**A**) Subnuclear distribution of MmpE-EGFP in transfected cells. Confocal microscopy
1064 was performed at indicated time points post-transfection. Nuclei were stained with
1065 DAPI (blue); MmpE-EGFP is shown in green. Scale bar, 10 μm. (**B**) Structural modeling
1066 of MmpE and NLS mutants. Predicted structures of wild type MmpE, NLS-deletion
1067 construct, and mutants lacking NLS1, NLS2, or both were generated using AlphaFold2.
1068 Models were visualized with UCSF ChimeraX, and prediction confidence was
1069 evaluated using pLDDT scores. **(C)** Immunoblot analysis of MmpE-Flag expression in
1070 bacterial lysates and culture supernatants from recombinant BCG strains. Ag85B and
1071 GlpX served as positive and negative controls for secretion, respectively. MmpE-Flag
1072 was detected with anti-Flag antibody. **(D)** Subcellular distribution of MmpE during
1073 infection. THP-1 macrophages were infected for 24 h with recombinant BCG strains
1074 expressing Flag-tagged wild-type MgdE or NLS-deletion mutants ($MmpE^{\Delta NLS1}$,
1075 $MmpE^{\Delta NLS2}$, and $MmpE^{\Delta NLS1\text{-}2}$). Cytoplasmic and nuclear fractions were prepared and
1076 analyzed by immunoblotting using anti-Flag antibody. Histone H3 and β-actin were
1077 included as nuclear and cytoplasmic markers, respectively.

A

PDB ID	Description	Z Value	RMSD Value
6py9-C	$Fe^{(3+)}$-$Zn^{(2+)}$ purple acid phosphatase	36.5	2.3
6py9-D	$Fe^{(3+)}$-$Zn^{(2+)}$ purple acid phosphatase	36.5	2.3
6py9-A	$Fe^{(3+)}$-$Zn^{(2+)}$ purple acid phosphatase	36.4	2.3
4kkz-C	purple acid phosphatase	36.3	2.3
4kkz-A	purple acid phosphatase	36.3	2.3
6g46-D	$Fe^{(3+)}$-$Zn^{(2+)}$ purple acid phosphatase	36.3	2.3
2qfp-B	purple acid phosphatase	36.3	2.3

Z value>10 and RMSD value<4 indicate that the comparison result is extremely reliable

B

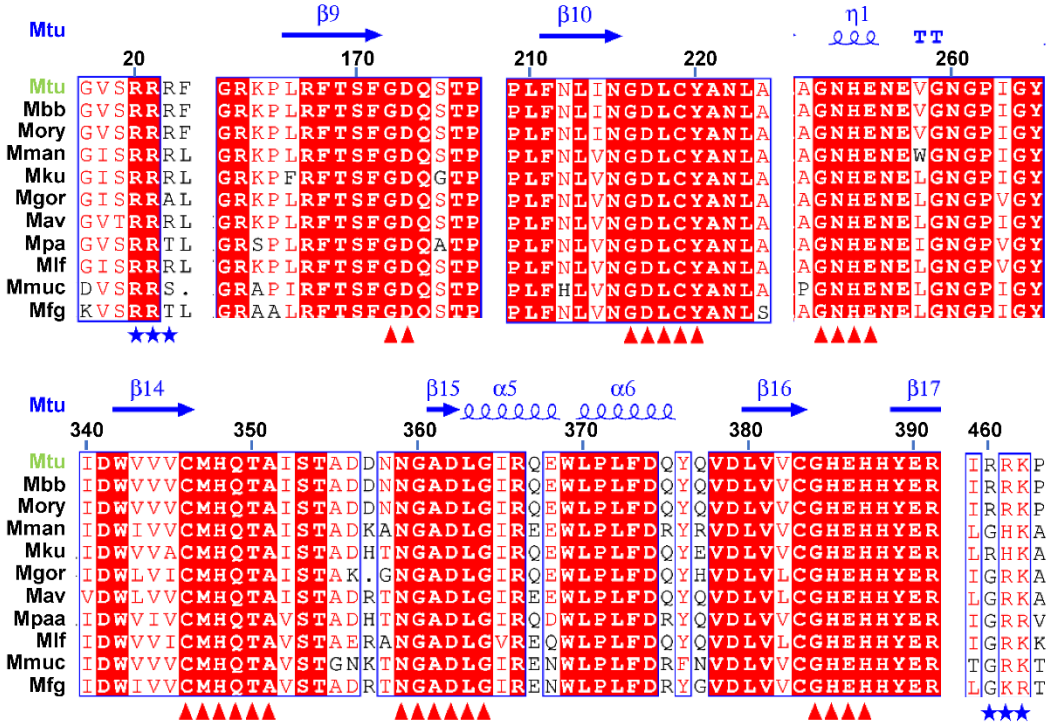

Supplementary Figure 2. Identification of MmpE as a conserved Fe^{3+}/Zn^{2+}-metallophosphatase in Mycobacteria.

(A) Sequence and structure-based analyses of MmpE. UCSF Chimera was used to analyze conserved domains and structural features. Structural similarity was evaluated by comparison with known metallophosphatases. Alignments with *Z*-scores >10 and RMSD <4 were considered high-confidence matches. **(B)** Clustal Omega sequence alignment of MmpE from various mycobacterial species, highlighting conserved

residues (≥90% identity, shown in red). Blue stars indicate the predicted NLSs, and red triangles mark characteristic sequences found in metallophosphatases. Species abbreviations: *M. tuberculosis* (Mtu), *M. bovis* BCG (Mbb), *M. orygis* (Mory), *M. kubicae* (Mku), *M. paraterrae* (Mpa), *M. farcinogenes* (Mfg), *M. mucogenicum* (Mmuc), *M. vicinigordonae* (Mgor), *M. lentiflavum* (Mlf), *M. avium* (Mav), *M. manitobense* (Mman).

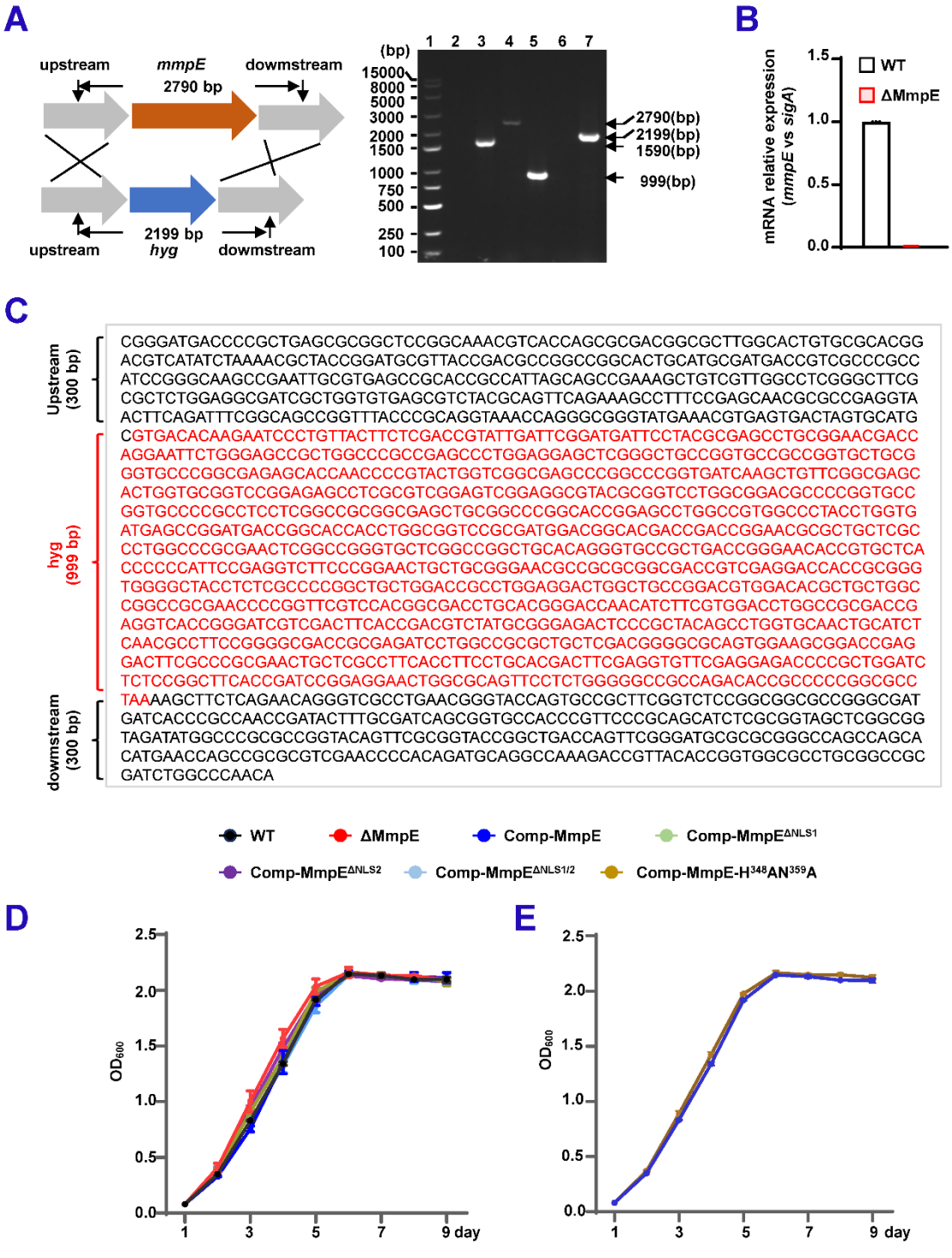

1093 **Supplementary Figure 3. The nuclear translocation and phosphatase activity of**
1094 **MmpE are essential for *M. bovis* BCG survival in macrophage cells.**
1095 (**A**) Construction and validation of the MmpE-deleted strain of BCG. (left) Schematic
1096 diagram of the homologous recombination strategy used to delete *mmpE* from the
1097 BCG genome. (right) Wild-type and ΔMmpE strains were used as templates to amplify
1098 the *mmpE* gene (600 bp upstream-600 bp downstream) by PCR. Lanes 1 and 3: wild-
1099 type genomic DNA; lanes 2 and 4: ΔMmpE genomic DNA. (**B**) qRT-PCR detected the
1100 *mmpE* expression level in WT and ΔMmpE strains. **(C)** Sequencing results of ΔMmpE
1101 genomic DNA. The forward primer amplified a 300 bp upstream fragment, and the
1102 reverse primer a 300 bp downstream fragment. (**D-E**) Growth curve analysis of BCG
1103 strains. Strains including WT, ΔMmpE, Comp-MmpE, Comp-MmpE$^{\Delta NLS1}$, Comp-
1104 MmpE$^{\Delta NLS2}$, Comp-MmpE$^{\Delta NLS1-2}$ strains(**C**), or Comp-MmpE-H348AN359H (**D**), were
1105 measured in 7H9 medium. Data represent mean ± SD of three independent biological
1106 replicates. Statistical significance determined using two-way ANOVA, *$P < 0.05$, **$P <$
1107 0.01, ***$P < 0.001$.

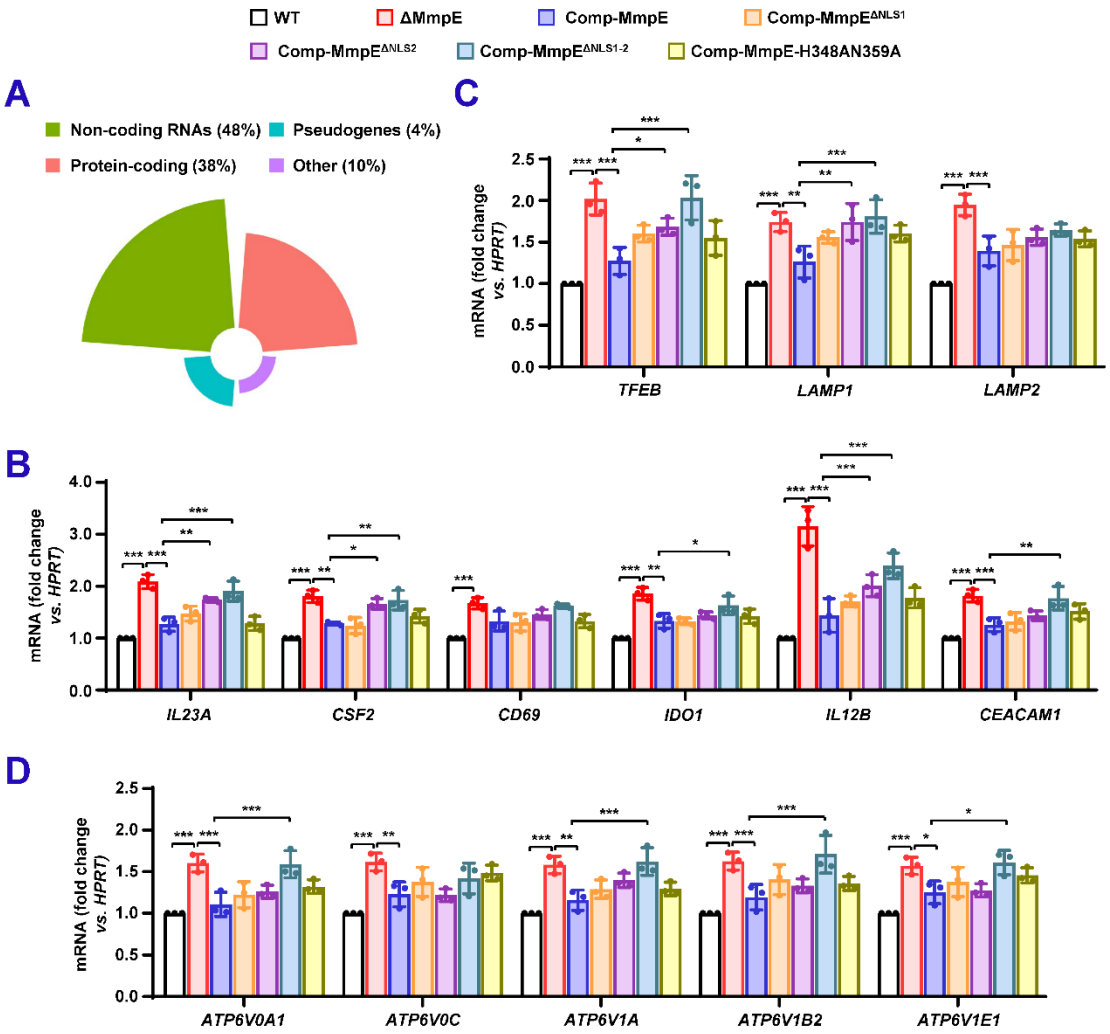

Supplementary Figure 4. MmpE modulates host transcription network involved in inflammation response and lysosomal maturation

(**A**) Biotype distribution of potential MmpE-regulating DEGs in THP-1 cells. (**B-D**) Quantitative RT-PCR analysis of gene expression in infected THP-1 cells. Cells were infected with WT, ΔMmpE, Comp-MmpE, Comp-MmpE$^{\Delta NLS1}$, Comp-MmpE$^{\Delta NLS2}$, Comp-MmpE$^{\Delta NLS1-2}$ and Comp-MmpE-H348AN359H strains for 24 hpi. Cytokine-related genes (*IL23A*, *CSF2*, *CD69*, *IDO1*, *IL12B*, *CEACAM1*) (**B**); genes associated with lysosomal maturation (*TFEB*, *LAMP1*, *LAMP2*) (**C**); genes encoding V-ATPase subunits (*ATP6V0A1*, *ATP6V0C*, *ATP6V1A*, *ATP6V1B2*, and *ATP6V1E1*) (**D**). Data represent mean ± SD of three independent biological replicates. Statistical significance determined using two-way ANOVA, *$P < 0.05$, **$P < 0.01$, ***$P < 0.001$.

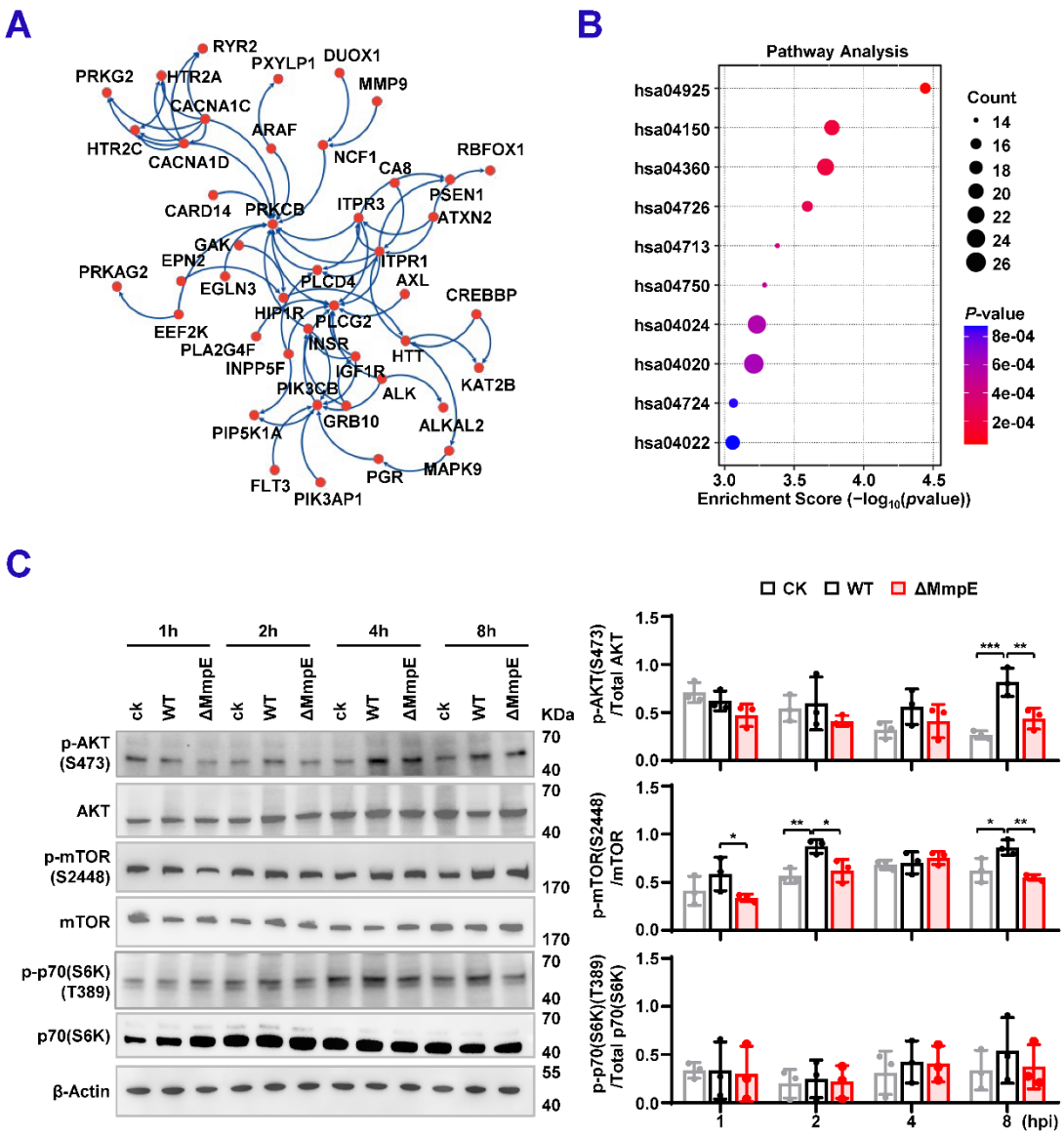

Supplementary Figure 5. MmpE regulates the PI3K-Akt-mTOR signaling pathway during macrophage infection.

(A) Interaction network of DEGs associated with MmpE-binding sites. The network was constructed using STRING v12.0 and visualized with Cytoscape. **(B)** KEGG pathway enrichment analysis of MmpE-binding sites identified in MmpE-EGFP-transfected HEK293T cells. Selected significantly enriched pathways are shown. Bar length indicates the number of associated genes; color represents -$\log_{10}$(*P*-value). Enriched pathways include aldosterone-regulated sodium reabsorption (hsa04925), mTOR signaling (hsa04150), axon guidance (hsa04360), serotonergic synapse (hsa04726), circadian entrainment (hsa04713), inflammatory mediator regulation of TRP channels (hsa04750), cAMP signaling (hsa04024), calcium signaling (hsa04020), glutamatergic

synapse (hsa04724), and cGMP-PKG signaling (hsa04022). **(C)** (left) Immunoblot analysis of PI3K-Akt-mTOR pathway activation in THP-1 macrophages infected with either wild-type (WT) or ΔMmpE strains. Phosphorylation of Akt (Ser473), mTOR (Ser2448), and p70S6K (Thr389) was assessed at 0, 2, 4, and 8 hpi. (right) Quantification of phosphorylation levels across time points. Data represent mean ± SD of three independent biological replicates. Statistical significance determined using two-tailed unpaired Student's *t*-tests, **P* < 0.05, ***P* < 0.01.

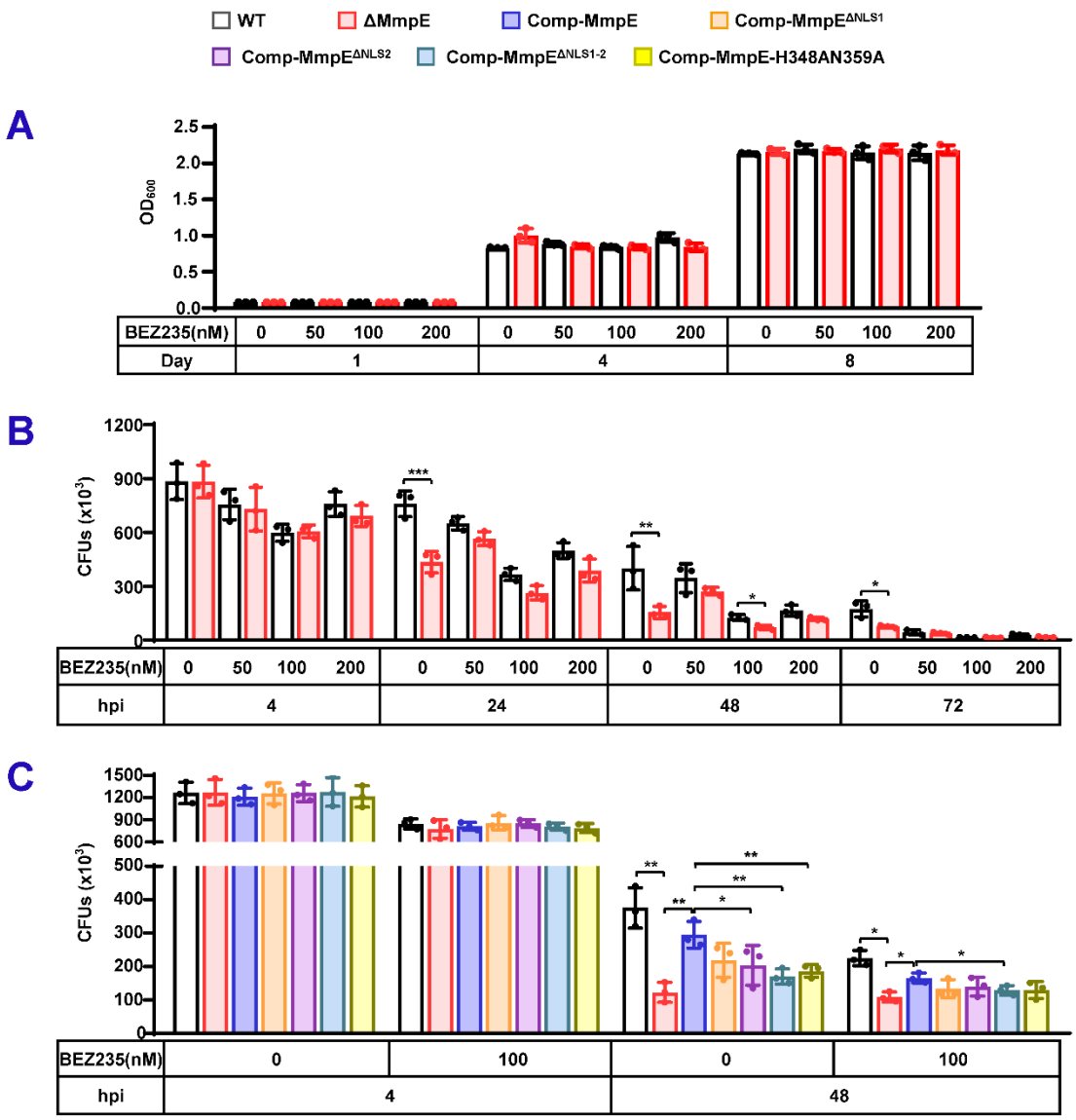

Supplementary Figure 6. MmpE promotes pathogen intracellular survival via the PI3K-Akt-mTOR signaling pathway.

(A-C) Effects of BEZ235 on the growth and intracellular survival of BCG strains.

1144 Bacterial growth in 7H9 medium with or without BEZ235 (0-200 nM) (**A**). Intracellular
1145 survival of WT and ΔMmpE strains in THP-1 macrophages treated with or without
1146 BEZ235 (0-200 nM); CFUs were quantified at 48 hpi (**B**). Intracellular survival of WT,
1147 ΔMmpE, Comp-MmpE, Comp-MmpE$^{\Delta NLS1}$, Comp-MmpE$^{\Delta NLS2}$, Comp-MmpE$^{\Delta NLS1\text{-}2}$,
1148 Comp-MmpE-H348AN359H in THP-1 macrophages treated with or without 100 nM
1149 BEZ235; CFUs were determined at 4, 48 hpi (**C**). Data represent mean ± SD of three
1150 independent biological replicates. Statistical significance determined using two-way
1151 ANOVA, *P < 0.05, **P < 0.01, ***P < 0.001.

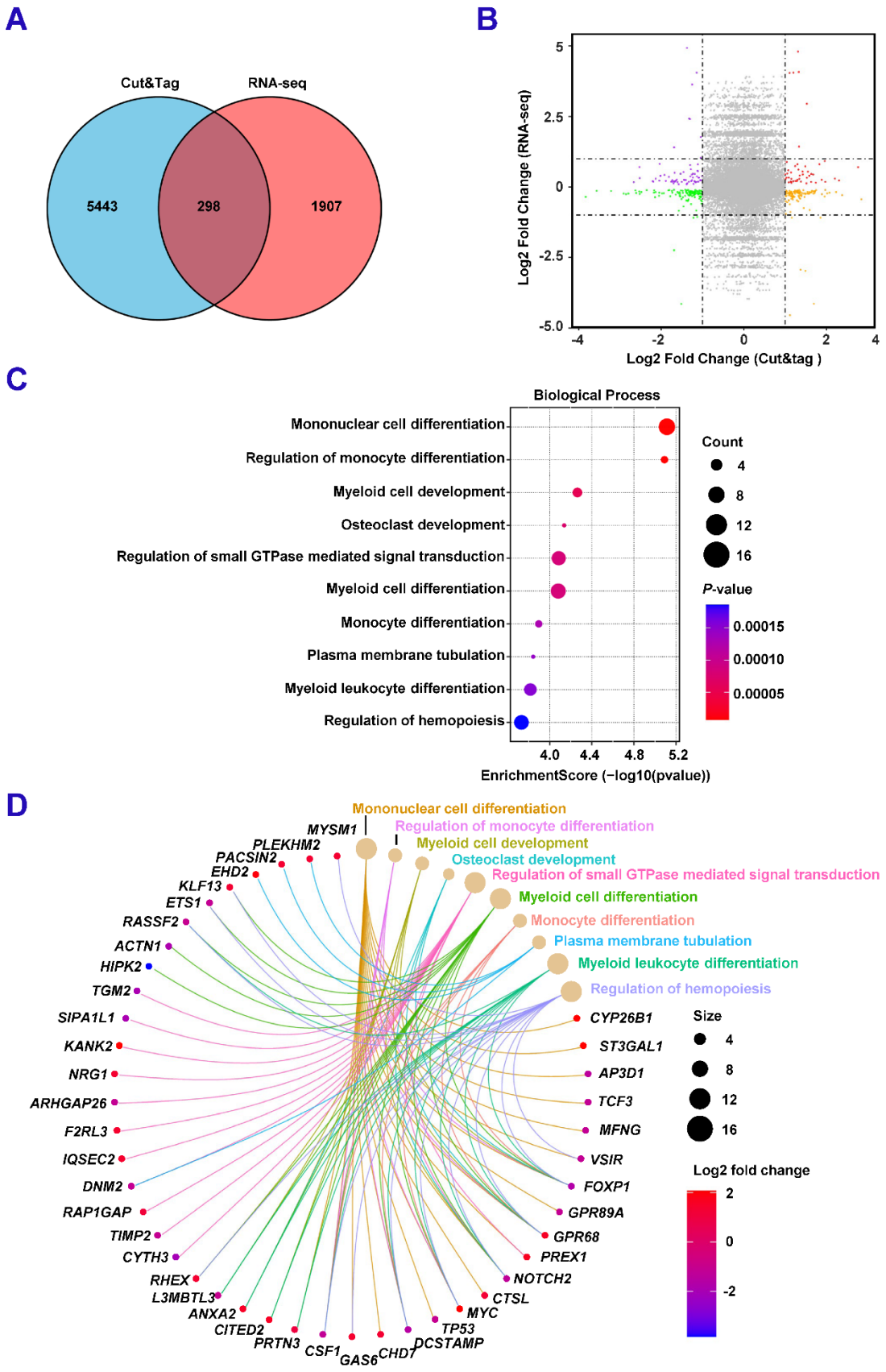

Supplementary Figure 7. MmpE modulates the transcription of immune-associated genes.

(A) Venn diagram showing the overlap between DEGs identified by RNA-seq and differential peak-associated genes identified by CUT&Tag-seq. **(B)** Four-quadrant scatter plot comparing CUT&Tag-seq and RNA-seq data. Log_2(fold change) values of peak-associated genes from CUT&Tag-seq are plotted against log_2(fold change) of FPKM values from RNA-seq. **(C)** KEGG enrichment analysis of the DEGs shown in **(A)**. **(D)** Chord diagram illustrating DEGs to enriched GO Biological Process terms.

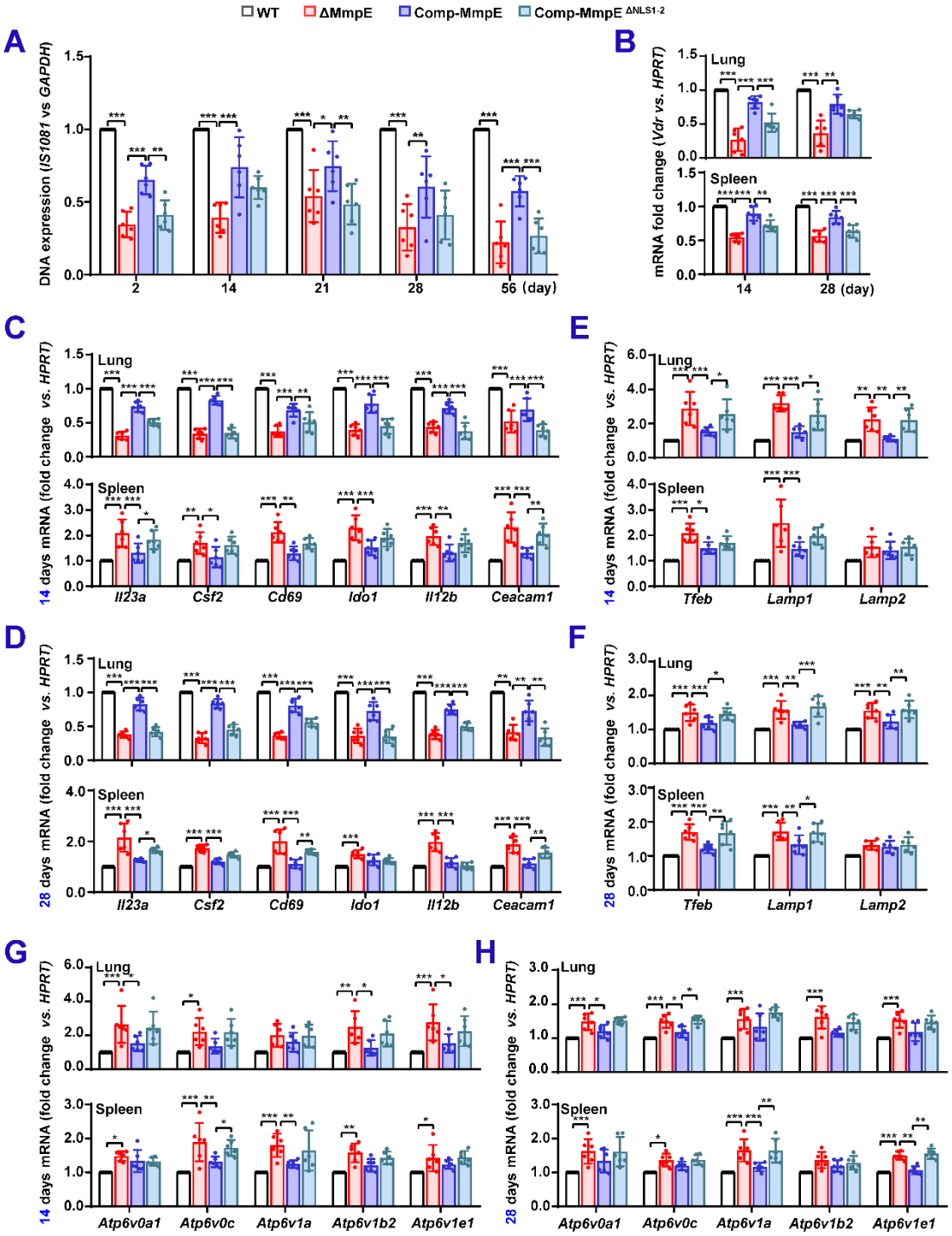

1162 **Supplementary Figure 8. MmpE facilitates bacterial colonization in the spleens**
1163 **of infected mice.**
1164 **(A)** Bacterial colonization was assessed in splenic homogenates from infected mice
1165 (as described in **Figure 7A**) by quantifying bacterial DNA using quantitative PCR at 2,
1166 14, 21, 28, and 56 dpi. **(B-I)** mRNA expression in mice spleen at 14 and 28 dpi in lung
1167 and spleen tissues of infected animals. *Vdr* expression (**B**); Cytokine-related genes (**C**
1168 and **D**); lysosomal acidification (**E** and **F**) and V-ATPase subunits genes (**G** and **H**).
1169 Data represent mean ± SD of six independent biological replicates. Statistical
1170 significance determined using two-way ANOVA, *$P < 0.05$, **$P < 0.01$, ***$P < 0.001$.